

# Monitoring Wind, Turbulence and Aircraft Wake Vortices by High Resolution RADAR and LIDAR Remote Sensors in all Weather Conditions

*Barbaresco F.\*, Thobois L. \*\*\*, Dolfi-Bouteyre A\*\*, Jeannin N. \*\*, Wilson R. \*\*\*\*, Valla M.\*\*, Hallermeyer A.\*\*, Feneyrou P. \*\*\*\*\*, Brion V. \*\*, Besson L. \*\*\*\*, Cariou J.P. \*\*\*, Leviandier L. \*\*\*\*\*, G. Pillet\*\*\*\*\*, Dolfi D.\*\*\*\*\**

\* THALES Air Systems, {frederic.barbaresco}@thalesgroup.com

\*\* ONERA, {agnes.dolfi-bouteyre, matthieu.valla, vincent.brion, nicolas.jeannin, alexandre.hallermeyer}@onera.fr

\*\*\* LEOSPHERE, {lthobois, jpcariou}@leosphere.com

\*\*\*\* LATMOS, Université Pierre & Marie Curie {richard.wilson, Lucas.Besson}@latmos.ipsl.fr

\*\*\*\*\* THALES Research & Technology, {patrick.feneyrou, luc.leviandier, gregoire.pillet, daniel.dolfi}@thalesgroup.com

Keywords: X-band RADAR, 1.5 micron LIDAR, wind, wake vortex, Eddy Dissipation Rate  
RADAR bande X, LIDAR 1.5 micron, vent, tourbillons de sillage, turbulence, EDR

## Abstracts

Air flows in the troposphere have a major impact on air traffic safety and operations. By air flows, several phenomena can be distinguished with different spatial and temporal characteristic scales: the mean wind itself, its rapid fluctuations, called turbulence, and wake vortices which are structured motions generated by each aircraft. At low altitudes, during take-off or landing phases, distance separations between aircrafts that limit today airport capacities were set up forty years ago to prevent the risk of wake vortices encounters in worst conditions. These out of date distance separations must be optimized since strength and lifetime of wake vortices vary a lot with weather conditions, like winds and turbulence. At high altitudes, during en-route flight phase, wake vortices as well as clear air turbulence can have a dramatic impact on aircraft safety. In this study, the way to measure wind, turbulence and wake vortices with new remote sensing techniques, 1.5 micron Coherent Doppler LIDAR, X-Band RADAR, and UV direct detection LIDAR, is detailed for ground-based or airborne applications. Sensor simulation tools and post-processing algorithms have been developed to retrieve wind, turbulence, especially EDR (eddy dissipation rate) and wake vortices parameters from sensors data and to assess their accuracy.

Les mouvements d'air dans la troposphère ont un impact important sur la sécurité aérienne et le trafic aérien. Plusieurs mouvements d'air peuvent être distingués comme le vent moyen, les fluctuations rapides de vent, appelées turbulence ou encore les tourbillons de sillage générés par chaque avion en vol. A basses altitudes, durant les phases de décollage et d'atterrissage, les distances de séparation entre avions, qui limitent aujourd'hui les capacités des aéroports, ont été établies il y a quarante ans afin de réduire le risque de rencontres de tourbillons de sillage dans les conditions les plus défavorables. Ces régulations peuvent être optimisées puisque la dangerosité des tourbillons de sillage dépend des conditions météorologiques comme le vent et la turbulence. A hautes altitudes, les tourbillons de sillage, ainsi que les turbulences en air clair, peuvent avoir un impact dramatique sur la sécurité des vols. Dans cette étude, les méthodes de mesures du vent, de la turbulence et des tourbillons de sillage par de nouvelles technologies de télédétection active de type LIDAR Doppler cohérent 1.5micron, RADAR Doppler bande-X et LIDAR UV à détection directe seront détaillées. Pour chaque paramètre cible, les outils de simulation et les algorithmes de post-traitement développés seront présentés ainsi que les précisions obtenues.

## 1. Introduction

Air traffic stakeholders will have to face to a doubling of the worldwide air traffic within the next twenty years, while, at the same time, they will have to improve safety and to reduce costs. To reach these objectives, atmospheric conditions and especially air flows in the troposphere must be better taken into account since they have a strong impact on air traffic operations.

At airports, during landing and takeoff phases, the overall runway throughput is limited by the risk of wake vortex encounter which are mitigated by the fixed and overly conservative ICAO wake turbulence separation minima defined forty years ago. This regulation determines for three aircraft categories the minimal distance separation between aircrafts

which allow to avoid the risk of wake vortex encounter for a follower aircraft at all time and whatever the weather conditions.

Wake vortices are created by all aircrafts in phase of flight behind each wing. They consist in two coherent counter-rotating flows, mostly horizontal spaced of  $b_0 = \frac{\pi}{4}b$  (typically 40m with  $b$  the wingspan) and equal of size (typically twenty meters). Their typical life times are usually comprised between one and three minutes.



**Fig. 1** - Initial vortices merging on two counter-rotating swirling flows.

Their strength is commonly characterized by their circulation, expressed in  $\text{m}^2/\text{s}$ , that induce rolling moment on a following aircraft. Circulation is computed on integrating the velocity on a disk of radius  $r$  centered on the vortex position as defined by the following formula:

$$\Gamma(x, t) = \int_0^{2\pi} \int_0^\infty V(x, r, \theta, t) r dr d\theta$$

To renew these out-of-date current regulations, many studies have firstly focused on the better understanding of the vortex structure and behavior especially with weather conditions. These studies have been successful thanks to the developments of new remote sensing technologies, like 1.5 micron Coherent Doppler LIDARs [1]. They showed that distance separations can be reduced thanks to in-depth statistical analysis of wake vortices measurements. For the wake vortices detection, LIDAR and RADAR sensors are complementary in terms of ambient weather conditions: X-band RADAR performances are optimal under rainy conditions when LIDAR performances are optimal in clear air. Wake vortices danger is highly influenced by atmospheric conditions. In case of cross winds, wake vortices will be transported out of the way of the oncoming traffic and thus will not represent any more danger. In addition, wake vortices decay will be quicker with high atmospheric turbulence. Theoretical analyses show that decay time of wake vortices is proportional to the cubic root of eddy dissipation rate (EDR).

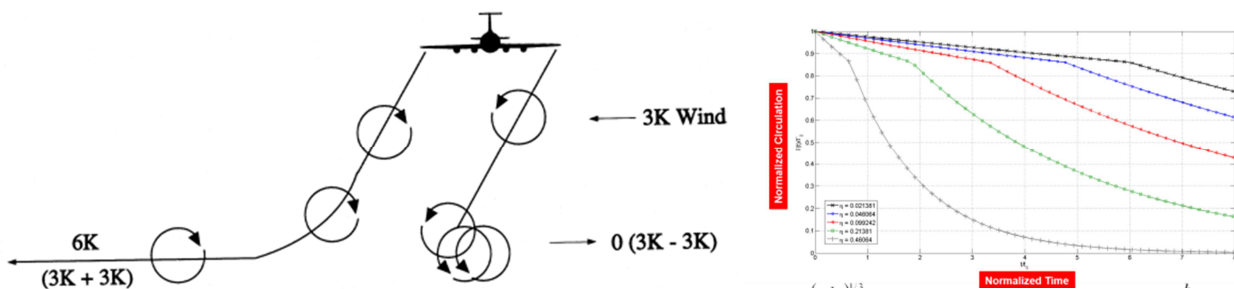


**Fig. 2** - Advection of wake vortices with crosswinds (left) and time evolution of dimensionless wake-vortex circulation with respect to dimensionless age indexed by dimensionless EDR – Courtesy of Pr Wickelmaers (right)

Since wake vortices behaviors vary significantly with atmospheric conditions, the highest airport capacities will be obtained with weather dependent distance separation concepts. The main principle consists in adjusting separation minima in real time with weather conditions and the development of operational Wake-Vortex Advisory System. In such a system, LIDAR and RADAR sensor technologies will be combined in a hybridized approach to mitigate wake vortices hazards in all weather conditions. These sensors are thus mandatory to provide accurate measurements of wind, turbulence and wake vortices around the airports and especially along the approach and take-off path below 500m, where the risks of wake vortex encounter are the highest, where air flows, especially wake vortices, cannot be accurately

predicted. It is important to remind that for Integrated Terminal Weather Systems, LIDAR and RADAR measurements are also useful to provide resolved 3D winds in all weather conditions that would allow to optimize air traffic operations.

At high altitudes, during en-route flight phase, wake vortices, can have also a dramatic impact on aircraft safety as well as clear air turbulence. The idea is then to be able to monitor these phenomena in advance in order to avoid the area of potential danger in measuring them from the aircraft by LIDAR and RADAR remote sensor technologies.

This paper will describe firstly the ground-based LIDAR and RADAR sensors that have been developed for measuring Wind, Turbulence and Wake vortices during landing, takeoff and en-route phases. The paper will then detail the developments of dedicated signal processing for 3D wind and EDR retrieval for a high power scanning 1.5micron coherent Doppler LIDAR, a 2D electronic scanning X-Band RADAR, a vertical X-band RADAR and a vertical 1.5micron coherent Doppler LIDAR used in the framework of the UFO project (Ultra-Fast wind sensOrs for wake-vortex hazards mitigation). Instrumental and atmospheric simulations used to validate and calibrate these algorithms will be presented. The applications of these algorithms on measurement campaigns will be detailed. Results are analyzed and compared with aircraft in-situ measurements and with weather prediction models, in order to assess the accuracy of the retrieved quantities. The paper will also considered the use of LIDAR and RADAR sensors for airborne measurements of clear air turbulence (CAT) and wake vortices for which different candidate technologies (RADAR, UV LIDAR, IR LIDAR) have been evaluated through simulations. Ground tests and Flight tests have been realized within FP7 project FIDELIO with an IR LIDAR for wake-vortices detection and with FP7 DELICAT with a UV LIDAR for CAT detection.

## 2. Ground-based LIDAR and RADAR sensors

### 2.1. Scanning 1.5 micron Coherent Doppler LIDAR

Scanning pulsed Doppler LIDAR (LIght Detection And Ranging) is the reference sensor for Wake Vortices measurements [3][4][5]. Coherent wind LIDARs are increasingly used for wind and turbulence assessment with applications in wind energy projects optimization, meteorology or aircraft security during take-off and landing [2]. Laser pulses are sent through the atmosphere and wind speed is measured using Doppler-induced frequency shift on the backscattered laser light. Laser sources with excellent spatial beam quality, narrow linewidth and typical pulse duration ranging from ~100 ns to 1  $\mu$ s are required. Pulsed master oscillator power all-fiber amplifier (MOPFA) are well adapted thanks to efficiency and robustness [2][3]. For coherent wind LIDARs, 1.54  $\mu$ m emissions of erbium/ytterbium fibers are used because of the good atmospheric transmission. Fiber lasers are versatile sources but with peak power limited to a few hundreds of Watts by stimulated Brillouin scattering (SBS) in standard fibers. Scanning pulsed Doppler LIDAR which is the reference sensor for Wake Vortices measurements [3][4][5], is used. The overall plan of a LIDAR is represented in Fig. 3 and its functioning described below:

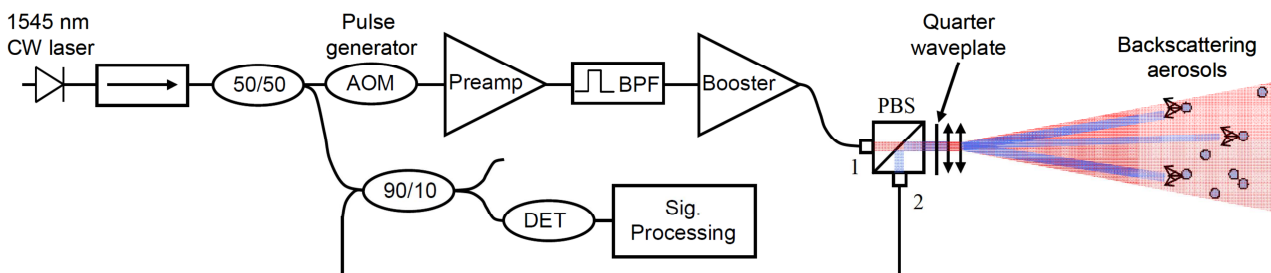


**Fig. 3 - Schematic optronics architecture of the 1.5micron coherent Doppler LIDAR based on fiber technology**

The master oscillator is a low-noise single-frequency fiber laser. A part of the energy is used for the heterodyne detection as local oscillator. On the other arm, an acousto-optic-modulator (AOM) is used as amplitude modulator and frequency shifter. Pulses are amplified up to 15  $\mu$ J in a fiber amplifier. Before the last high power amplifier stage, a bandpass filter is used to suppress the amplified spontaneous emission (ASE) in previous amplifier. Pulse energy and peak power are limited by the SBS at 200  $\mu$ J and 300 W respectively in the high power Erbium/Ytterbium large mode area (LMA) fiber amplifier. We applied an optimal strain distribution using a patent pending device to the active fiber in order to increase the SBS threshold. Pulses with 370  $\mu$ J energy (corrected from ASE) at 10 kHz repetition frequency, 820 ns duration and 450 W peak power have been achieved. The  $M^2$  is less than 1.3 in both axes. Polarization extinction ratio was measured higher than 20 dB. The main limitation of this high power laser source is the ASE created in the last amplifier, that reaches 30 % of the total output power. In the state of the art, kilowatt peak power with 500 ns was achieved with similar laser architecture [4] but with larger linewidth seeder (800 kHz). Higher peak power (up to 630 W) was achieved with 400 ns pulses.

This new high peak power laser source developed by ONERA has been integrated inside a LEOSPHERE Windcube Scanning LIDAR deployed at Toulouse for UFO project trial Fig. 22 in order to achieve long range (>10km) wind measurement.

## 2.2. 2D Electronic Scanning X-Band RADAR

THALES has developed an X-band Solid-State Electronic Scanning Radar, entitled in Airport Watcher demonstrator. Airport Watcher radar is a new generation airport weather X-band radar to be installed on fixed locations close to runways. Its main missions are to monitor wind hazards in terminal airport area (<500 m in altitude), and more specifically wake-vortex hazards close to runways on final approach (from < 100 m in altitude to the threshold). This demonstrator has also been defined to monitor 3D Wind and EDR (Eddy Dissipation Rate) in the glide slope until 10 km (500 m in altitude for a glide slope of 3°) and rain rate retrieval until 60 km (instrumented range).

Thanks to its capacity of Electronic scanning in elevation, Airport Watcher radar can scan the glide for the last 100 m in altitude at High Update-Rate, every 7.5 seconds and monitor wake-vortex in 3D (azimuth, elevation range). Its High Range resolution of 5 m, achieved by Pulse compression, allows discriminating each roll-up, separated initially of 3/4 of aircraft wingspan. Its High Doppler resolution can accurately monitor wind fields in each vortex.

Complementary to the main mission, Airport Watcher is able by waveforms interleaving, simultaneously plays secondary missions: retrieval of accurate wind fields, retrieval of EDR (Eddy Dissipation Rate) to characterize atmospheric turbulence, retrieval of Rain Rate by reflectivity.

Airport Watcher is designed around high performances Hardware Full solid-state 600 W modular transmitter enabling graceful degradation of the transmitter. Airport Watcher Radar has an electronic beam steering antenna. This antenna has been designed for wake-vortex monitoring at range lower than 2 km. Main characteristics of the antenna are: slotted Waveguide, with Beamwidth (azimuth x elevation)  $1.8^\circ \times 1.8^\circ$ , of 40 dB directivity. The radar is made of 3 parcels: The radar Cabinet / Drive / Antenna.

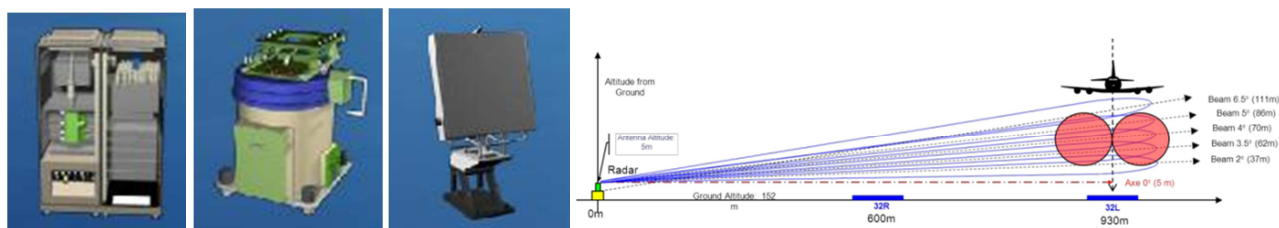


**Fig. 4** – (on the left) Cabinet/Drive/Antenna parcels, (on the right) Electronic scanning in elevation



**Fig. 5** – THALES airport watcher X-band Radar Demonstrator on Paris-CDG Airport



## 2.3. Vertical X-Band RADAR

In recent years, LATMOS (Laboratoire Atmosphères, Milieux, Observations Spatiales) has developed a new X-band Doppler mini-RADAR named CURIE (Canopy Urban Research on Interactions and Exchanges) [6]. This small RADAR (see Fig. 6), with a low consumption of 70 W, aims at describing the dynamics of the low atmospheric boundary layer (ABL), especially in urban environments. CURIE is a pulsed coherent X-band RADAR with a frequency of 9.42 GHz. The pulse duration is 150ns with a repetition period of 2.4 $\mu$ s. If required, CURIE can be used as a wind profiler with a parabolic antenna pointing only in the vertical direction only. The received signal is amplified, down-converted, filtered and then sampled at the intermediate frequency of 60~MHz. Generation of the pulsed emitted signal, digital reception, coherent integration and decoding are programmed in a FPGA (Field Programmable Gate Array). Doppler spectra (4096 FFT points) are calculated from I and Q time series lasting 3 or 6 s, depending on the number of coherent integrations (150 or 300). Spectra are obtained for altitudes ranging from 40 m above ground level to 720~m, the vertical resolution being 22.5~m.



*Fig. 6 - Parabolic Antenna of the CURIE RADAR on a roof of a shelter (left) and View of the WINDCUBE7v2 LIDAR (right)*

## 2.4. Vertical 1.5micron Doppler LIDAR

The WINDCUBE7v2, developed and manufactured by the LEOSPHERE company, is a pulsed and coherent (heterodyne) LIDAR emitting infrared (IR) radiations (1.54micron) in five beams directions, one vertical and four 28° off-vertical [7]. Measurements consist in radial velocities inferred from the Doppler shift of the light backscattered by atmospheric aerosols. Radial velocities are measured with a time resolution of 0.8 s, a complete cycle being thus obtained in four seconds. The LIDAR can provide 12 wind measurements from 40m to 200m with a resolution of 20m and an accuracy of 0.1m/s.

## 3. Post-processing algorithms and simulation tools for retrieving Wind, EDR and Wake vortices with LIDAR and RADAR sensors

### 3.1. Wind retrieval

Doppler LIDARs and RADARs provide as a basic product the radial wind data thanks to the measurement of Doppler frequency shift along the beam propagation path. The radial wind data corresponds to the projection of the wind vectors on the beam and thus they don't represent the orthogonal winds to the beam. In order to retrieve all the components of the wind, that is to say headwind and crosswind for air traffic operations, specific algorithms have been developed to combine the radial wind speeds at different range gates and different azimuth angles provided by a Scanning Doppler LIDAR or RADAR in using multiple PPI (Plan Position Indicator) scanning patterns at various elevation angles. Various

wind retrieval algorithms exist to compute 2D and 3D vector fields from Doppler LIDAR or RADAR radial data from Volume Velocity Processing (VVP) [8] to 2DVAR [9] or 4DVAR methods. Other hybrid approaches have been developed more recently that combine VVP and data assimilation techniques [10][11][12]. For the RADAR, the VVP algorithm will be used whereas for the LIDAR, the hybrid technique based on VVP and single decomposition value will be employed.

### 3.2.EDR Retrieval

#### 3.2.1. Methods

If wind retrieval methods are well known and widely used for post-processing RADAR or LIDAR data, EDR retrievals remain a relative new topic especially for addressing operational purposes as air traffic applications. Doppler LIDARS and Doppler X-band RADARS can provide information about wind field spatial statistic and then give an estimation of the turbulence or Eddy Dissipation Rate [13][14][15][16]. The estimation can be made from

- Doppler Spectrum width,
- Velocity Variance, or
- Velocity Structure function

EDR estimation algorithms, although using different processing techniques, all rely on Power spectral representations of turbulence. In this approach, the power spectrum density of the velocity fluctuations in the inertial range has a universal shape based on the Kolmogorov theory.

$$S_w(k) = c \alpha_k \epsilon_k^{2/3} k^{-5/3}$$

Where  $k$  is a radian wavenumber,  $c$  is a constant equating 1 for longitudinal velocity fluctuations, and  $4/3$  for transverse velocity fluctuations.

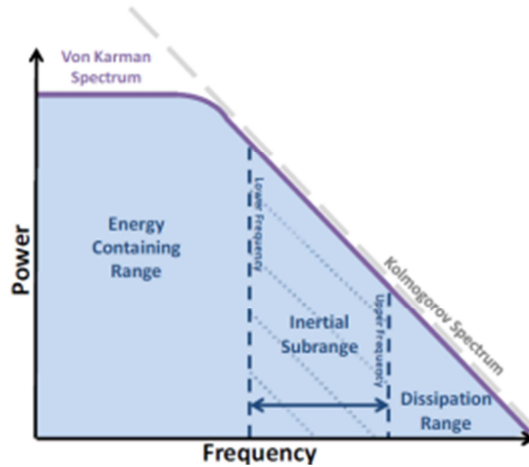


**Fig. 7 - Power spectra representation of turbulence in a log-log plot**

The general idea is to fit the Kolmogorov Spectrum in the inertial sub-range. There are no set values for the upper and lower frequencies of the inertial sub-range, and the frequency range may vary in different atmospheric conditions and at different altitudes.

#### • EDR Retrieval by Doppler Spectrum Width

The Doppler Spectrum width  $\sigma_v^2$  can be used only if the spectral broadening is mainly due to the turbulence velocity fluctuations  $\sigma_T^2$  or if the other causes of broadening ( $\sigma_B^2$ ) are corrected (beam width  $\sigma_\theta^2$ , shear broadening  $\sigma_S^2$ , broadening due to non-turbulence fluctuations  $\sigma_{NT}^2$ ) [17][18][19].  $\sigma_T^2 = \sigma_v^2 - \sigma_B^2$

After these corrections, EDR, noted  $\epsilon$ , can be estimated from measurement data with the following formulas:

$$\sigma_{\theta}^2 = \theta_1^2 / 16 \ln 2 \quad \theta_1 \text{ is the one-way angular resolution (i.e., beamwidth)}$$

$$\sigma_r^2 = (0.35 c \tau / 2)^2 \quad \text{where } c \tau / 2 \text{ is the range resolution}$$

$$\text{If } r \cdot \sigma_{\theta} < \sigma_r \quad \text{then } \varepsilon \approx \left[ \sigma_v^3 / \sigma_r (1.35 A)^{3/2} \left[ \frac{11}{5} + \frac{4}{15} r^2 \sigma_{\theta}^2 \right] \right]^{-3/2}$$

$$\text{If } \sigma_r < r \cdot \sigma_{\theta} \quad \text{then } \varepsilon \approx 0.72 \cdot \frac{\sigma_v^3}{r \cdot \sigma_{\theta} A^{3/2}}$$

With  $1.53 < A < 1.68$

For RADARs, the beam broadening must be subtracted from the Doppler spectrum width to obtain the turbulence broadening. EDR can be inferred by noticing that the observed broadening results from the convolution of turbulent velocity fluctuations with the RADAR illumination function • [21] • [22] • [23]. Finally, EDR is given by:

$$\varepsilon = \sigma_T^3 \left( \frac{4\pi}{\alpha_K} \right)^{3/2} J^{-3/2}$$

Where  $\alpha_K = 0.52$  a Kolmogorov constant and J an integral depending on the mean horizontal wind and on the dimensions of the RADAR volume • [27]. The integral J has to be numerically integrated.

#### • EDR Retrieval by Velocity variance or frequency spectra

If the temporal sampling is sufficient, time series of radial velocities can be built • [24] • [25] • [26]. The EDR is then directly calculated from the velocity variance  $w_{rms}$  following:

$$\varepsilon[Var] = 2\pi \left( \frac{2}{3c\alpha_k} \right)^{3/2} \frac{(w_{rms}^2)^{3/2}}{L_l}$$

Where  $\alpha_k = 0.52$  a Kolmogorov constant, c is a constant equating 1 for longitudinal velocity fluctuations, and 4/3 for transverse velocity fluctuations,  $L_l$  is the scale of the largest turbulent eddies, i.e.  $L_l = V_H T$ , T being the duration of the time series,  $V_H$  the horizontal wind.

An alternative method consists in computing the velocity spectrum in the inertial subrange with the knowledge of the horizontal wind:

$$\varepsilon_k[S] = \frac{2\pi}{V_H} \left( \frac{f^{5/3} S_v(f)}{c\alpha_k} \right)^{3/2}$$

where  $f$  is frequency ( $s^{-1}$ ). This method is mostly adapted to vertical profilers which are pointing the same volume with a high frequency.

#### • EDR Retrieval by Structure Function

This method has been used for retrieving EDR from scanning LIDARs • [13] • [14] in evaluating the structure function of the radial velocity as a function of azimuth angle. It takes into account the filtering by the laser pulse length and signal

analysis window length. This procedure enables high vertical resolution for EDR profiling and a high sensitivity to scales that are less than the effective range resolution in the transverse structure function calculation.

The velocity fluctuation  $\hat{v}'$  at each point in the space  $(R, \theta)$  is taken to be the difference between the measured radial velocity  $\hat{v}$  and the fitted mean velocity  $\bar{v}$  :

$$\hat{v}'(R, \theta, k) = \hat{v}(R, \theta, k) - \bar{v}(R, \theta, k)$$

The longitudinal structure function is then calculated using velocity fluctuation:

$$D_v(s) = \langle [\hat{v}'(R, \theta, k) - \hat{v}'(R + s, \theta, k)]^2 \rangle$$

Where the summation is made over all the possible ranges and scans over 3 minutes, and  $s$  refers to separation on meters. If the fluctuations of the radial velocity are homogeneous and isotropic over the plane, a simple model for the structure function can be defined:

$$D_v(s) = 2\sigma^2 \Lambda(s/L_0)$$

Where  $\sigma^2$  is the variance of the radial velocity,  $\Lambda(x)$  is a universal function, and  $L_0$  is the outer scale of turbulence.

For the von Karman model, the universal function  $\Lambda(x)$  is defined as:

$$\begin{aligned} \Lambda(x) &= 1 - \frac{2^{2/3}}{\Gamma(1/3)} x^{1/3} K_{1/3}(x) \\ &= 1.0 - (0.5925485) x^{1/3} K_{1/3}(x) \end{aligned}$$

Where  $K_{1/3}(x)$  is the modified Bessel function of order 1/3.  $\Gamma(z)$  is the Gamma function.

The Kolmogorov model is valid for small separation ( $s < L_0$ ) and for isotropic turbulence [38][37]. The velocity spectrum is the Fourier transform of the two point velocity correlation function. Within this inertial sub-range, the energy spectrum of velocity follows the Kolmogorov spectra. The EDR value is then obtained by fitting either the 2/3 slope for the structure function. The output value is often  $\epsilon^{1/3}$  ( $\text{m}^{2/3} \cdot \text{s}^{-1}$ )

$$D_v(s) = C_v \epsilon^{2/3} s^{2/3}$$

Where  $\epsilon$  is the energy dissipation rate and the Kolmogorov constant  $C_v \approx 2$ .

### 3.2.2. Simulations

In order to test and validate the EDR retrieval algorithm for LIDAR and RADAR, a 2D turbulent wind field simulator has been developed. This 2D turbulent isotropic wind field simulator is based on 2D Von Karman spectrum formulas [20]. The simulator generates 2D Gaussian white noises, applies spectrum, cross spectrum weightings and inverse fast Fourier transforms to yield the turbulent wind fields with Von Karman statistics. Fig. 8 shows an example of turbulent wind field realization, over a field of 1500 m by 1500m, for a given EDR level and turbulence scale  $L_0$ .



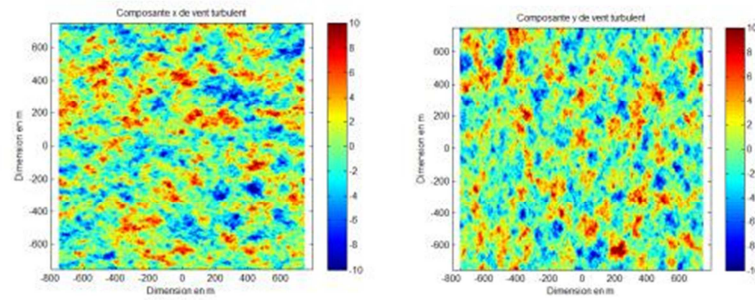


**Fig. 8** - ONERA simulator generating a 2D isotropic and homogenous turbulence, for a given value of EDR and turbulent scale. Horizontal wind component is on the left and vertical wind component is on the right.

To determine the influence of range resolution on the estimation of the EDR calculated with structure function algorithm for LIDAR and RADAR, simulations are performed for three range resolutions EDR (10m, 20m, and 50m) and three EDR (light (0.003), moderate (0.01), severe (0.1)).

For a RADAR sensor, the results obtained are displayed on Fig. 9. In red dashed line the theoretical EDR in input simulation and in blue line, the estimate EDR calculated with structure function algorithm:

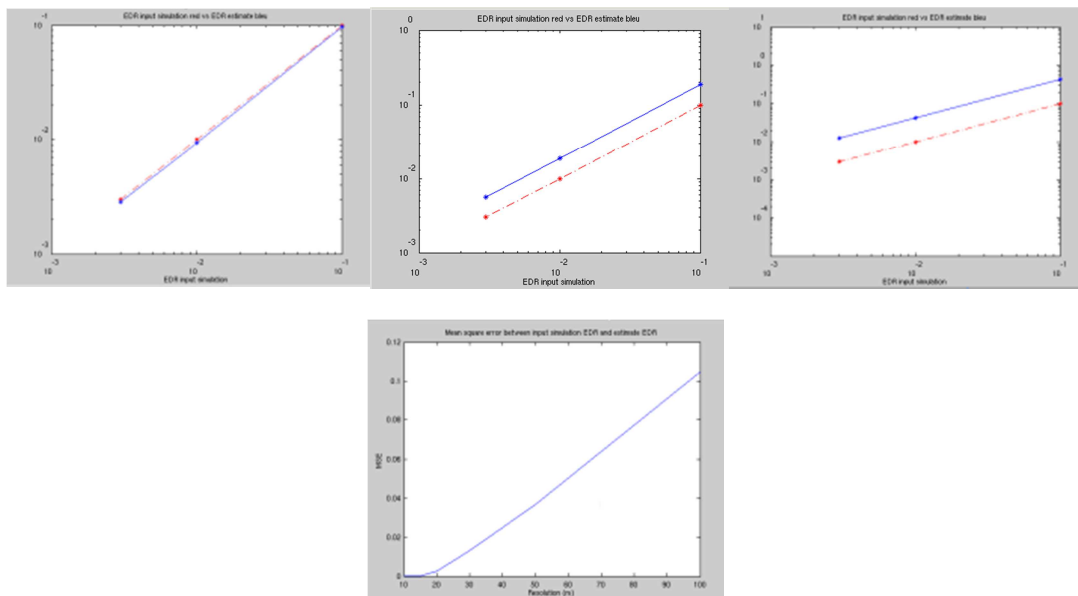


**Fig. 9** - Comparison between EDR input simulation and estimated EDR for range resolution 10m/20 m/50 m (at right)  
Mean Squared Error with respect to resolution

It can be inferred that range resolution has a significant influence on EDR estimation with structure function. Thus, the algorithm of EDR calculation with the structure function should be used with RADARs that have a small resolution; lower than 20m or the bias should be corrected since it is proportional to the range resolution.

The same kind of simulations is performed for retrieving EDR from LIDAR data. Fig. 10 shows that the LIDAR as all remote sensor acts as a low pass filter in regards to high frequency turbulence structures. The structure function fit has been performed for different wind field realization at different EDR values, without and with LIDAR filtering.

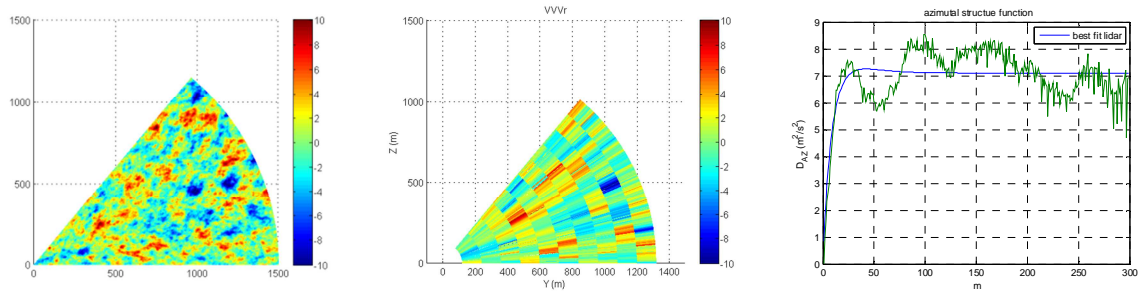


**Fig. 10** - Left : radial component on LIDAR axis, Middle : LIDAR response. Right :example of azimuthal structure function and it's best fit. Color scale is the velocity in m/s.

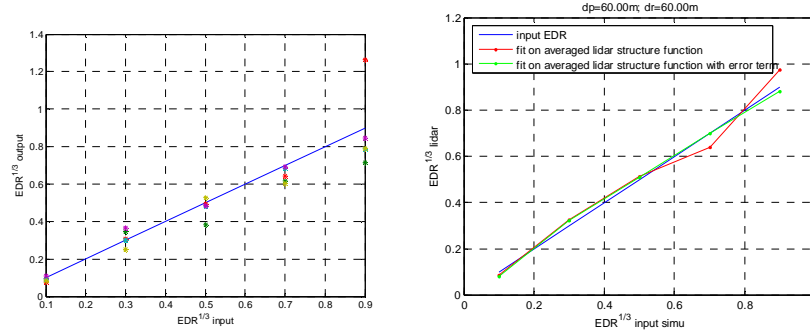


**Fig. 11** - EDR retrieval on different wind field realizations at different EDR values. Left : without LIDAR . Right : with LIDAR response and using averaged structure function (with and without the error term).

As discussed above, in the case of homogeneous and isotropic turbulence, the Kolmogorov hypothesis states that within the inertial sub-range the statistical representation of the structure function  $D_{\epsilon}(s)$  is given by previous equation. To verify the accuracy of this model on our LIDAR data, we plotted on the same graph the structure function calculated previously and the Kolmogorov model in Fig. 11 for different range resolution. As for the RADAR, range resolution of the LIDAR has a direct impact on the accuracy on EDR retrievals. Similarly, a correction term can be applied in order to calibrate the EDR values and thus reducing the range resolution effect on EDR.

### 3.3.Wake vortices retrievals

#### 3.3.1. X-band RADAR signature Model & Simulation of Wake-Vortex in Rainy Weather and in clear air

##### RADAR signature in rainy weather

The detection by X band RADAR of wake vortices in rainy weather cases is a much easier task than in clear air due to the higher levels of signal. In fact the raindrops are backscattering a significant fraction of the transmitted energy (proportional to the 6<sup>th</sup> power of the electric radius of the raindrops in a first approximation). In the vortex air flow, raindrop's trajectories are disturbed with regards to their free fall trajectories. This modification of the trajectory induces a modification of the Doppler spectrum. To assess the modification of this Doppler spectrum, a model based on raindrops' cinematic assuming generic vortex air flows has been developed in [28]. It relies on the computation of the modification of the drop size distribution in the vicinity of the vortex. This concentration of rain drops is computed through a box counting approach, seeding uniformly distributed raindrops above the vortex and assessing the modification of raindrops residence time at any neighbourhood in the vicinity of the vortex illustrated on Fig. 12 -.

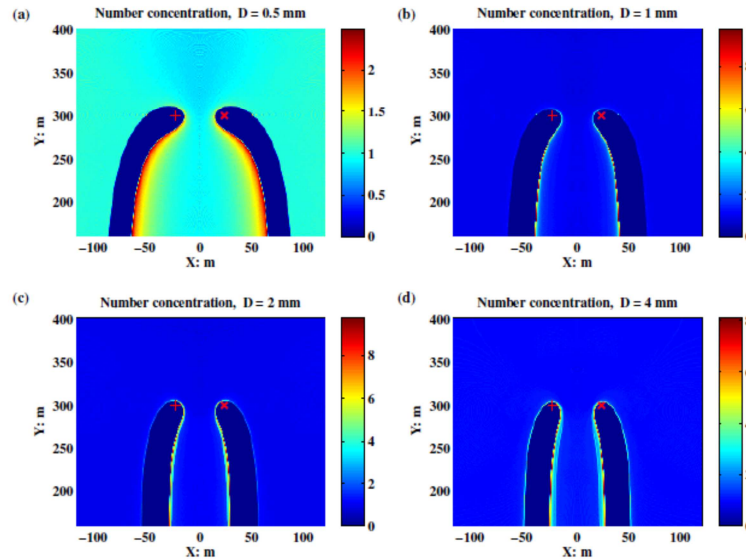


**Fig. 12** - Modification of raindrops size distribution function of the diameter of the drops.

The presence of the vortex tends to result in areas with lower drops concentration around and below the vortices and a higher concentration between the vortex cores. To be able to reconstruct the Doppler spectrum in a later stage, the probability distribution of the velocity components of the raindrops by class of diameter is also tabulated.

After the computation of the modification of the drop size distribution, the simulations are done firstly by choosing the parameterization of the vortex air flow, the RADAR characteristics (frequency, resolution, pointing direction with regards to the axis of the vortex), and the weather parameters (i.e the rain rate and the drop size distribution). Then, in each RADAR resolution cell, the reflectivity in the wake vortex region is computed by integrating the contribution of each class of raindrop modulated by the modification of its concentration due to the vortex flow. The Doppler spectrum is then obtained through a similar methodology by sorting the contributions of the drops by classes of radial velocities as illustrated on Fig. 13 - Range Doppler spectrum simulated considering the modeling and a generic wake vortex generated by an A380 with a 1 mm/h rain rate. The RADAR is pointed orthogonally to aircraft trajectory.

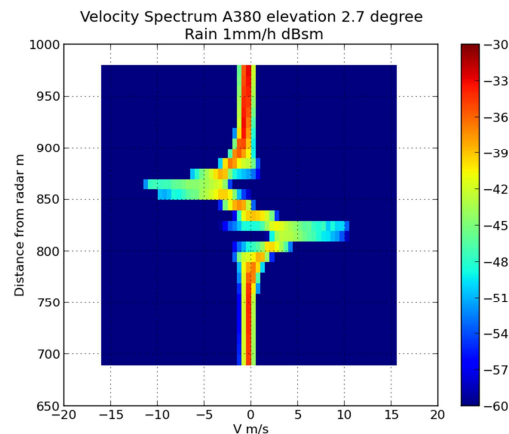


**Fig. 13** - Range Doppler spectrum simulated considering the modeling and a generic wake vortex generated by an A380 with a 1 mm/h rain rate. The RADAR is pointed orthogonally to aircraft trajectory.

The characteristics of the vortices cannot be deduced directly from the analysis of the measured Doppler moments as the velocity of the droplets differs from the one of the flow due to their non negligible weight. However, they could be compared to a set of simulated signatures with known vortex characteristics, to look up for the most likely situation. To get a better idea of the discrimination capabilities of detection and characterization algorithm, the Doppler spectrum of

raindrops due to the natural background turbulence should be integrated within the simulations. The model has so far been applied to rain drops but could be applied similarly to the case of fog or snow. In this case the measured speeds will be closer to the ones encountered in the air flow. Nevertheless at X band the reflectivity will be significantly lower and for measurement purposes a shift towards W band could be of interest.

### RADAR signature in clear air

In clear air RADAR signals are returned from wake vortices as a consequence of Rayleigh scattering. In the absence of water droplets, the mixture of molecules associated with clear air (mostly gas molecules of diazote  $N_2$ , dioxygen  $O_2$  and water vapor  $H_2O$ ) sees its distribution of electrons modified by the electromagnetic waves transmitted by the RADAR. The capacity of displacement of these electrical charges under the Coulomb force, called the polarizability of the molecule, generates induced dielectric moments whose vibrations at the RADAR frequency act as local sources of electromagnetic waves. As a consequence a part of the incoming wave is scattered by the flow in every direction of space. Although the polarizability of these molecules is low, positive RADAR response of wake vortices have been reported in a number of past experiments [29]. In this section a numerical model of the scattering of RADAR waves by trailing vortices is provided and used to evaluate the RADAR Cross Section of the wake vortices in clear air. The method couples in a one-way sense the Navier-Stokes and the Maxwell equations, with the first set dictating the thermodynamic state of the flow and the second set describing how the electromagnetic waves propagate and scatter. The approach is based (i) on a laminar description of the flow obtained by Direct Numerical Simulations (DNS) of the Navier-Stokes equations in a sectional plane of the vortices at moderate Reynolds numbers and (ii) on the direct integration of the response due to the polarized electromagnetic dipoles present in the flow using the Born approximation. The field of refractive index  $n$ , which makes the link between the Navier-Stokes and the Maxwell equations, depends on the thermodynamic state of the flow following

$$(n - 1) \times 10^6 = 223 \rho_d + 299 \rho_v + 1.74 \times 10^6 \frac{\rho_v}{T}$$

In the Thayer's relation,  $\rho_d$  and  $\rho_v$  are the mass density of dry air and water vapor and  $T$  is the temperature. The first two terms in Thayer's formula correspond to the induced polarizability of dry air and water vapor, and the third term corresponds to the permanent polarizability of the water vapor.

The flow model is based on the Boussinesq approximation which takes advantage of the low Mach number of the flow and of the small vertical extent of its evolution (typically a few wingspans). The flow dynamics is governed by the following equations, given in normalized quantities

$$\begin{aligned} \nabla \mathbf{u}^* &= 0 \\ \frac{d\mathbf{u}^*}{dt} &= -\nabla p^* + N^{*2} \theta^* \mathbf{e}_z + Re^{-1} \nabla^2 \mathbf{u}^* \\ \frac{d\theta^*}{dt} &= -\mathbf{u}_z^* + Re^{-1} \nabla^2 \theta^* \\ \rho^* &= -\theta^* \end{aligned}$$

The Reynolds number, given by  $Re = \frac{V_0 b}{\nu}$ , measures the strength of the viscous effects in the flow, and  $N^*$  is the normalized Brunt-Vaisala frequency. Here we consider the case of the Kwajalein experiments [29] for which  $N^* = 0.79$ . The aircraft generating the wake is a C5-A of circulation  $\Gamma_0 = 390 m^2/s$ , span  $b = 68 m$  and a characteristic time  $t_0 = 46 s$ . The flow is simulated for a Reynolds number equal to 5000, in a two-dimensional configuration, a situation that yield purely laminar flow. **Fig. 14** presents the temporal evolution of the field of refractive index associated with the flow. In particular the background refractive index variations related to the atmospheric gradients are not shown.

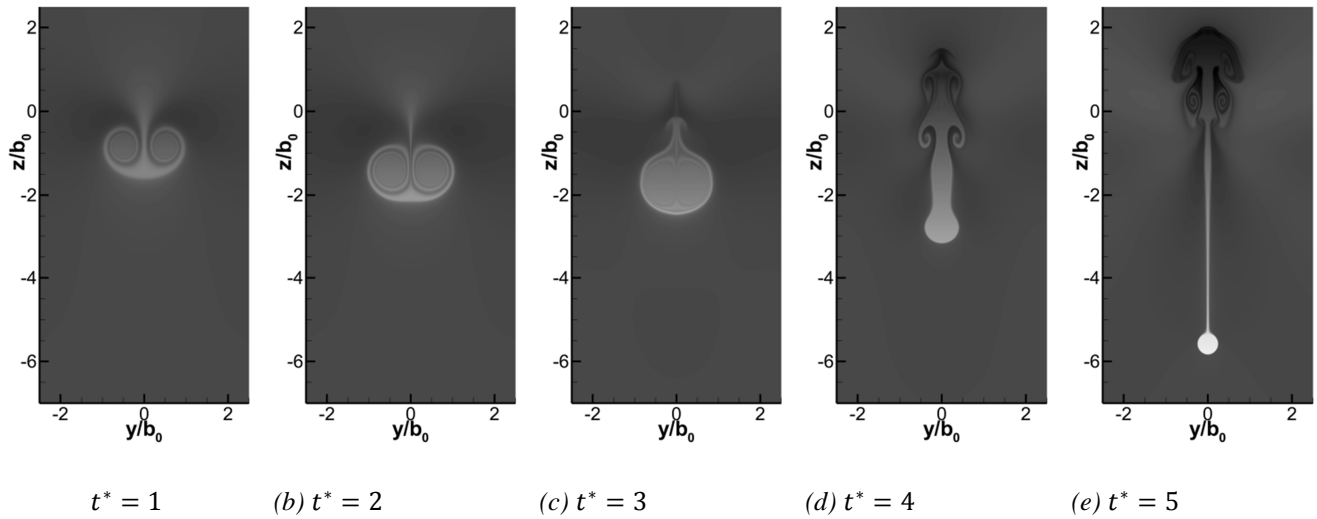


**Fig. 14 -** Field of refractive index (normalized) obtained from simulation at  $Re = 5000$  seen at different times.

The evolution of the vortices over 5 characteristic times of the initial flow shows several effects. Note that time  $t^*$  is time normalized on  $t_0$ . The vortex pair descends as a result of its momentum. The field of refractive index is modified both by the vortex descending motion and by the baroclinic torque induced by the atmospheric stratification. As a result, the size and the form of the patch of refractive index greatly varies during the evolution of the flow. At early times the structure of the refractive index is that of two spirals formed by the entrainment of the surrounding stratified fluid by the vortices. At later times, the patch associated with the vortices become quite small, and almost uniform, and a second zone, located above the vortex pair, appears (this structure is usually referred to as the secondary wake) and extends from the primary wakes up to a position located above the aircraft flight path (at  $z = 0$ ).

Once the field of refractive index is obtained, the electromagnetic problem is solved using the Maxwell equations with a constant magnetic permeability  $\mu_0$  and a variable dielectric constant  $\epsilon$ , in the absence of free charges and for time harmonic fields. These equations yield

$$\begin{aligned}\nabla \cdot \mathbf{E} &= \frac{\rho_{eq}}{\epsilon_0} \\ \nabla \cdot \mathbf{B} &= 0 \\ \nabla \times \mathbf{E} &= j\omega \mathbf{B} \\ \nabla \times \mathbf{B} &= -j\omega\mu_0\epsilon_0\mathbf{E} + \mu_0\mathbf{J}_{eq}\end{aligned}$$

where

$$\begin{aligned}\rho_{eq} &= -\frac{\epsilon_0}{\epsilon} \mathbf{E} \cdot \nabla \epsilon \\ \mathbf{J}_{eq} &= -j\omega\epsilon_0\epsilon_r\mathbf{E}\end{aligned}$$

are the equivalent charge and current distributions associated with the polarization of the medium. The scattered electric and magnetic fields are obtained following

$$\begin{aligned}\mathbf{E}_s(\mathbf{r}) &= \nabla \times \nabla \times \int_{V'} \epsilon'_r(\mathbf{r}') \mathbf{E}_i(\mathbf{r}') \frac{e^{jk|\mathbf{r}-\mathbf{r}'|}}{4\pi|\mathbf{r}-\mathbf{r}'|} d\mathbf{r}' \\ \mathbf{B}_s(\mathbf{r}) &= -j\omega\epsilon_0\mu_0 \nabla \times \int_{V'} \epsilon'_r(\mathbf{r}') \mathbf{E}_i(\mathbf{r}') \frac{e^{jk|\mathbf{r}-\mathbf{r}'|}}{4\pi|\mathbf{r}-\mathbf{r}'|} d\mathbf{r}'\end{aligned}$$

Note that  $\epsilon'_r$  is the refractive index due to the wake vortices only. The RCS is obtained by making a budget of the electromagnetic power transmitted by the target (here the wake vortices) and received from it. The mean power transmitted by the target is  $P_b = \sigma \overline{S_i} \cdot l$  where  $S_i$  is the power flux density associated with the incident field,  $\sigma$  is the

target RCS and the over bar denotes the time average. Similarly the average power flux received is  $P_r = \overline{S_s \cdot o}$ . The flux density is related to the electric and magnetic fields by the Poynting vector

$$\mathbf{S} = \frac{1}{2} (\mathbf{E} \times \mathbf{H}^*)$$

Where  $\mathbf{H}^*$  denotes the complex conjugate of the magnetic field. The definition of the RCS follows

$$\sigma = 4\pi r^2 \frac{\overline{S_s \cdot o}}{\overline{S_i \cdot i}}$$

The numerical calculation of the scattered electric and magnetic fields is performed for the wake vortices of Fig. 14. The RADAR operates in backscattering mode at normal incidence. The atmospheric conditions are those of the Kwajalein experiments as described in [30]. The relative humidity is  $RH_0 = 7\%$ , and the beam aperture is  $\theta_b = 2.37^\circ$ . The RADAR is at a horizontal distance  $R_R = 15\text{km}$  from the aircraft which flies at an altitude of 5000ft. The elevation angle of the RADAR beam, which points to the aircraft altitude, is  $\beta = 5.8^\circ$ . The wake is measured after 66s, which amounts to  $t^* = 1.4$  in normalized time units. At this instant, the simulation indicates that the vortices have descended over a vertical distance of  $\Delta z \simeq -1.2b_0$ . According to Fig. 14 the flow is in the stage where it rolls-up the surrounding stratified fluid, and the refractive index fluctuations have a spiraling pattern. The reference value of the dielectric constant is  $|\epsilon_r'| = 1.3 \times 10^{-6}$ . Fig. 15 shows the numerical results obtained in the range  $kb_0 \in [0.1, 500]$ . The wake RCS is maximum in the low frequency range which corresponds to the scales present in the flow. These scales comprise that of the coherent wake (that scales on  $b_0$ ) and those associated with the spirals (that are fractions of  $b_0$ ). This explains the occurrence of multiple peaks in the RCS distribution. Higher frequencies for which the flow features no fluctuations, reflects residual values associated to the numerical scheme, and are not physical. This numerical experiment shows that laminar structures in the flow associated with wake vortices produce RCS at low frequencies with maximum levels of  $-50\text{dBm}^2$ . The analysis of the flow response at higher frequencies would require the incorporation of turbulent scales in the flow. Owing to Bragg scattering, the turbulent scales are the only one able to generate finite RCS in the RADAR bands currently investigated for wake vortex monitoring systems such as X-band or higher.

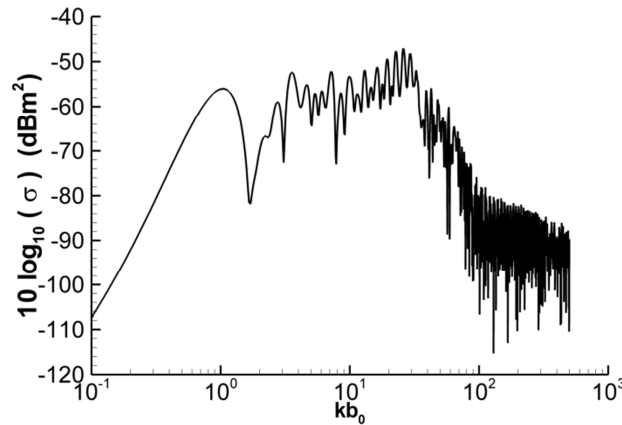


Fig. 15 - RADAR Cross Section of the wake vortices shown in Fig. 14 as a function of the normalized wavenumber.

### 3.3.2. Wake vortices measurements with LIDAR in clear air

Scanning Pulsed Coherent Doppler LIDAR are considered as the reference sensor for wake vortex detection and characterisation since they have been widely used for more than one decade to support the understanding of wake vortices behaviours and the developments of new concepts of distance separations [31][32][34]. There are two families of algorithms that exist to extract useful information from LIDAR spectra.



- The first one is based on extracting velocity envelopes using a threshold that depends on the SNR and so needs to be adapted by the user. The frequencies at the first intersection points on each side of the main peak (upper and lower) between this threshold and the spectral density are retrieved and converted into velocities (negative and positive). The envelope is then obtained for each Range Gate by representing these two values of velocity according to the angle index of the corresponding LOS. Then, in order to compute the circulation, different methods are exploitable like integrating the envelope at the range of the vortex core between 5 and 15 meters called  $\Gamma_{5-15}$  [31][35]
- The second family gathers the algorithms making use of the maximum likelihood estimation (MLE) with a Wake Vortex model chosen among all the existing ones like Hallock- Burnham or Lamb-Oseen. The parameters to estimate are generally the Wake Vortices circulation and their positions. Different approaches and variant can be listed in the literature. The solution proposed by Frehlich(2005) [36] using the Hallock-Burnham model at first considers the pair of vortices as a single system where they both have the same altitude and circulation which leaves 3 parameters (altitude, distance to the vortex pair center and circulation) to estimate. Then, when the vortices diverge due to mutual interactions and ground effects, each one is considered as an independent system with its own position and circulation which requires to estimate no more 3 but 6 parameters.

Computing time for the second family (MLE) is longer and more used in post processing whereas first family is preferred for real time display. In order to optimize LIDAR architecture and to test LIDAR signal processing algorithms, a LIDAR response model is used.

The first step of the simulation is to compute the Doppler frequencies associated with the velocities of the aerosol particles. In order to simulate a 2D turbulent wind field with a given EDR level algorithm, an algorithm based on Morin and Yaglom [37] work has been developed. For wake vortex wind field generation, different model exist such as Hallock-Burnham or Proctor models.

These velocities are then projected on the LIDAR axes that are the Line Of Sights (LOS) since the only ones that are accessible thanks to the LIDAR measurement are the radial velocities  $v_r$ . Once projected, the corresponding Doppler frequencies can be calculated with the laser wavelength and the LIDAR reference frequency  $f_{IF}$  thanks to (3).

$$f_d = f_{IF} - \frac{2v_r}{\lambda} \quad (3)$$

Once computed, the Doppler frequencies are the inputs of a LIDAR simulator using a feuilleté model [7]. This simulator that has been validated by several measurement campaigns also takes in input, signal processing, optical, electronic, scan and atmospheric parameters such as the sampling duration, the transmitter and receiver pupil radius, the sampling frequency or the back scattering coefficient and yields the accumulated periodograms of each range gate of each accumulated line of sight.

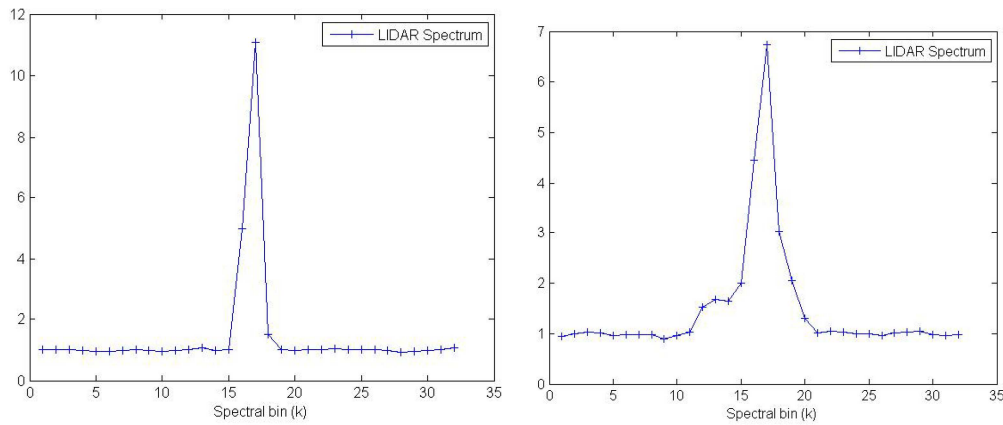


**Fig. 16 - Exemple of LIDAR spectrum (left) without any wake vortex, (right) in presence of wake vortex**

## 4. Ground based Measurements campaigns with LIDARs and RADAR

### 4.1. Paris Charles de Gaulle Airport Trials for wake vortex measurements

During XP1 trials campaign of SESAR P12.2.2 project at Paris CDG Airport, a multifunction X-band RADAR (wake-vortex, weather, traffic) with Electronic scanning capability and a Scanning 1.5micron Coherent Doppler LIDAR have been deployed in September/October 2012 for simultaneously monitor Wake-Vortex close to the runways.

The X-band RADAR was localized 830 m perpendicular to the glide slope of runway 26L on the South-East area of CDG Airport according to the configuration in **Fig. 17**. With an update rate lower than 10 s, wake-vortex waveform was instrumented until less than 4 km, with a spatial resolution of 5 m, and Doppler resolution lower than 1 m/s.

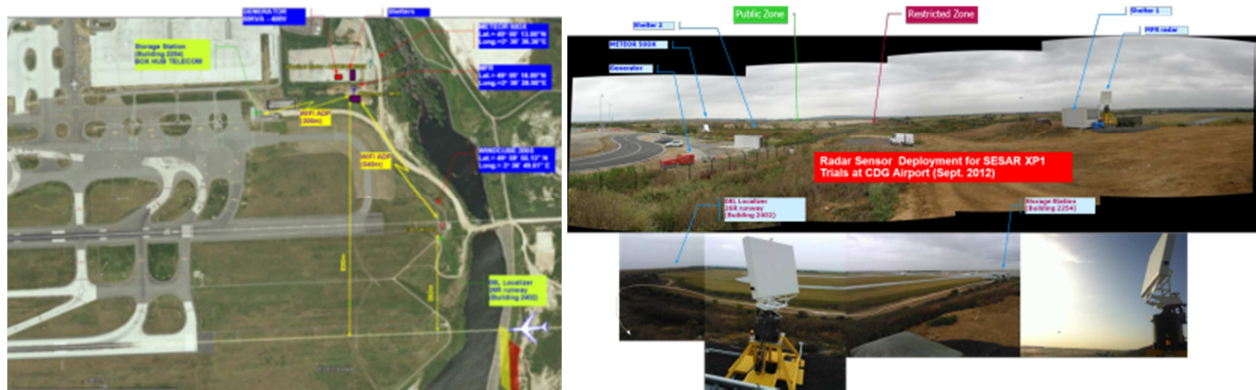


**Fig. 17** - X-band Electronic-scanning AIRPORT WATCHER demonstrator RADAR Deployment at Paris CDG Airport for SESAR project, (at left) map of sensor deployment 830 m from the glide, (at right) RADAR site close to runway

In vertical scanning mode, individual roll-up of each wake vortex were tracked in range and elevation axes. In **Fig. 18**, above the first nearer runway, wake vortex generated by aircraft during departure has been observed. These detections of wake vortex are coherent with classical behavior close to the ground. Each roll-up from scan to scan (with one scan every 7.5 seconds) can be tracked as proved by the trials. Close to the ground, trajectory of each roll-up can finely and accurately been followed and their strength been estimated by circulation assessment. The wake vortex RADAR detection is based on a Doppler analysis of raindrops signature, whose raindrops trajectory and distribution are driven by the wind flow induced by the two counter-rotating wake vortices. Raindrops act partially as tracers biased by their terminal speed velocity (size distribution vary with rain rate). According to the Biot-Savart Law, the local flow velocity could be computed at sum of each roll-up contribution (modeled as velocity profiles). The RADAR was able to detect wake vortices in all kind of rain, from drizzle to heavy (which is fully complementary to the LIDAR performances), with a detection sensitivity at 2 km of  $-16$  dBZ. In following figure(**Fig. 18**), the 3D monitoring capability by Electronic scanning RADAR is illustrated. We give 3D azimuth/elevation of Mean Doppler Spectrum for successive scans every 7.5 seconds. We can observe the wake-vortices transport by cross-wind and oscillations in last scans generated by crow instability.

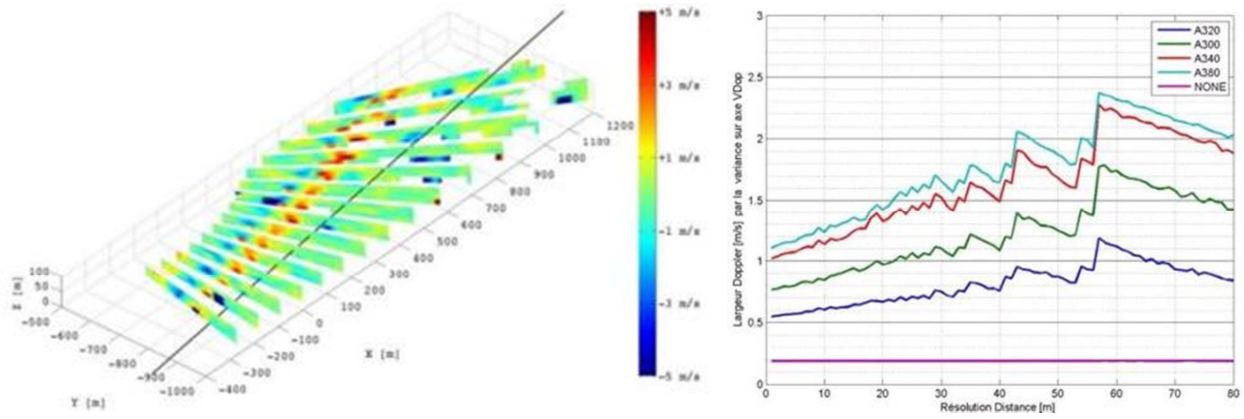


**Fig. 18** - (at left) 3D monitoring of Mean Doppler velocity on successive scan with an update rate of 8 seconds, (at right) Simulation of Doppler Spectrum Width computed on averaged spectrum of all beams

One of the most attractive conclusions in ONERA/SAE PhD Thesis is that the Doppler spectrum width of raindrops is representative of the wake vortex circulation. as vortex circulation decreases, the Doppler spectrum width of raindrops narrows. To consolidate these results, THALES has used simulators to correlate Wake-Vortex Circulation with Doppler Spectrum width, computed by averaging the Doppler Spectrum of all beams in elevation and by variation of Range resolution. We have simulated wake-vortices Doppler signature with a distance RADAR-to-runway of 930 m for 5 beams in elevation  $2^\circ/3.5^\circ/4^\circ/5^\circ/6.5^\circ$  of 4 aircraft categories (A320, A300, A340, A380). The glide slope is intercepted at the altitude of 68 m. Results have been averaged for 3 rain rates: 1 / 5 / 20 mm/h.

In previous figure (**Fig. 18**), we illustrate the Doppler Spectrum Width, estimated by variance of Doppler velocity computation, for different Range resolution. We have previously averaged Doppler Spectrum on successive beams in elevation. We can observe that the Doppler spectrum width is a good indicator for wake-vortex circulation retrieval that preserves the order between aircraft categories: Doppler Spectrum Width for a Range resolution of 50 m: (A380) 1.9 m/s > (A340) 1.7 m/s > (A300) 1.25 m/s > (A320) 0.85 m/s > (rain) 0.2 m/s. We should also take into account influence of EDR on results. In previous simulations, EDR had not been simulated.

If we neglect bias induced by rain droplets inertia, we can compute a more accurate relation between Doppler Spectrum moments and Wake-Vortex Circulation, as done by Rubin for RASS system. If we consider  $S(V_i)$  the spectral magnitude of a Doppler velocity bin, after previously applying CFAR on Doppler axis to extract Doppler peaks in spectrum and threshold to eliminate noise, it can be proved that the Circulation is proportional to moment at power  $2/3$  :

$$\Gamma \propto \left[ 2 \int_{V_{\min}}^{V_{\max}} V_i^2 [S(V_i)]^{2/3} dV_i \right] / \left[ \int_{V_{\min}}^{V_{\max}} [S(V_i)]^{2/3} dV_i \right]$$

More, recently, the X-band AIRPORT WATCHER RADAR demonstrator with electronic scanning antenna has been installed at Paris CDG Airport close to North runways pairs.

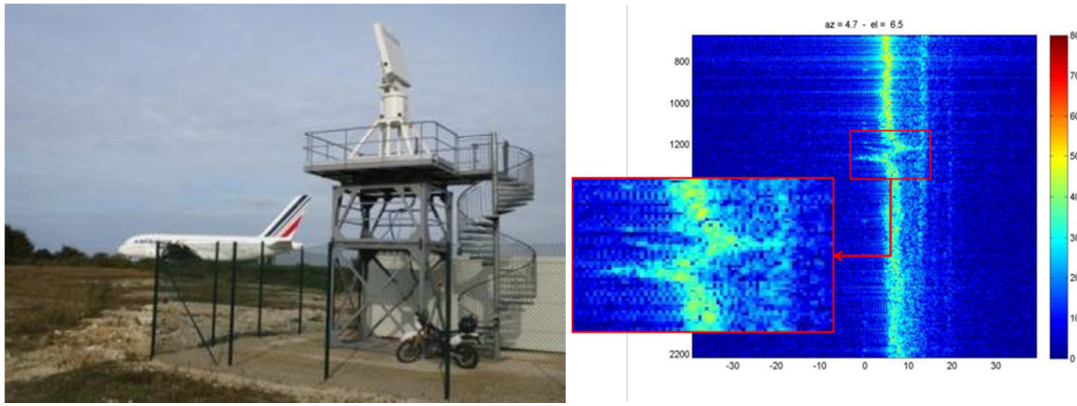


**Fig. 19** (at left) X-band AIRPORT WATCHER RADAR demonstrator with electronic scanning antenna deployed at Paris CDG Airport, (at right) Zoom on Doppler Spectrum of wake vortices for beam at elevation 6.5°

Within European SESAR P12.2.2 project, Doppler LIDARs have been deployed in two trials occurred in May 2011 (XP0) and October 2012 (XP1). During those measurements campaigns, a 1.5 $\mu$ m LEOSPHERE scanning Doppler LIDAR and Thales X-band RADAR have been successfully tested. The LIDAR is a 1.54  $\mu$ m fibered coherent Doppler LIDAR delivering an average output power of 1 Watt. The pulse length is 200ns, as a compromise between velocity resolution and range resolution and is adapted to the application (wind measurement or wake vortex measurement). The scanning angular resolution depends on the scenario. For IGE vortices detection, the angular resolution is about 0.5 m/rad. During XP0, real time display of the average wind field was performed. The positions of wake vortex cores and circulations calculations were automatically post processed. A range resolution of 4 m for wake vortex detection was obtained by overlapping the larger range gates defined by the pulse length. The goal of XP1 was to achieve real time wake vortex monitoring. Therefore, real time processing of wake vortex has been implemented thanks to a range resolution limited to 8 m (4 m when post processing), the implementation a. narrow track windows driven by the vortex motion due to the cross wind, parallel processing and GPU card use . The percentage of detection is 86 %. Most undetected events were during rainy period. Because wake vortices were IGE, they were followed during 2 scans in most cases. But, the wind was often in the LIDAR direction pushing the vortex towards it. Then on this typical example one vortex is rapidly destroyed while the other one rebounds and is transported by the wind, hence the greater observation time, e.g. up to 90 s.

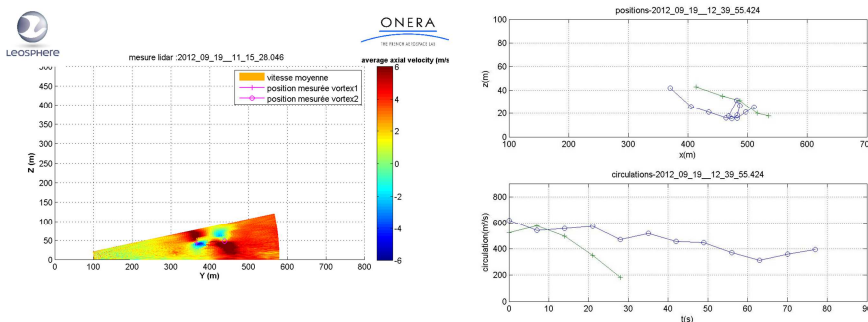


**Fig. 20** : wake vortex measurements with Doppler LIDAR during XP0 trial . left : mean wind field , with wake vortex localization . right up , example of inground effect wake vortices trajectories , right bottom , circulation measurement as a function of time for the two vortices .

## 4.2. UFO project Toulouse Trials for wind and EDR measurements

A two month campaign has been performed at Toulouse-Blagnac airport in April to May 2014 in order to demonstrate the capabilities of the Scanning 1.5micron Coherent Doppler LIDAR, the 2D Electronic Scanning X-Band RADAR, the Vertical X-Band RADAR and the vertical 1.5micron Doppler LIDAR to retrieve wind and EDR in the framework of the



UFO project. The sensors were installed on the East of the airport in order to monitor at 360° around the airport and the glide path for the scanning devices.

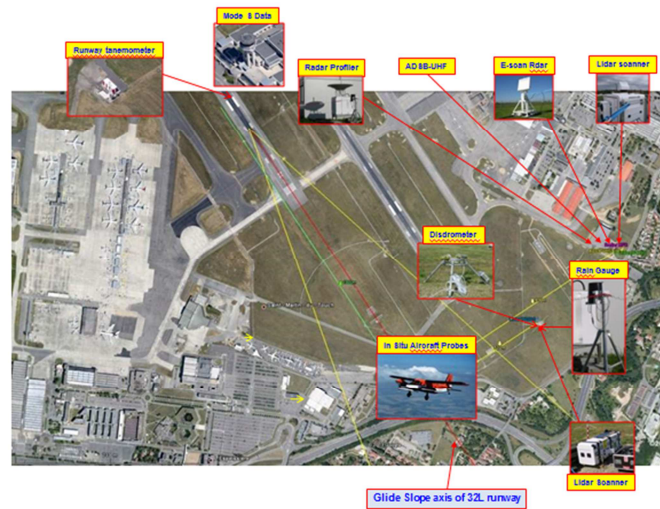


**Fig. 21** – Setup of the sensors at Toulouse-Blagnac airport

The 1.5micron fiber-based high power laser scanning LIDAR displayed below has been configured in order to perform wind and EDR measurements every kilometer along the glide path in less than one minute. A sequence of several PPI scanning patterns has been determined to ensure the theoretical accuracy of wind and EDR retrievals and the fastest update rate as possible. Typical accumulation times of 0.16s were used per line of sight to allow the measurement range of the WINDCUBE scanning LIDAR up to 10km.

In addition, wind retrievals algorithms have been applied to provide volume and glide path wind data around an airport up to 10 km (correspond to the requirement of 500 m in altitude for a slope of 3°) on the Toulouse data collection. Compared to a reference, the agreement in terms of bias and standard deviation for the horizontal wind speed (respectively 0.37m/s and 0.59m/s) is good.



**Fig. 22** – Picture of the Windcube Scanning LIDAR deployed at Toulouse (left) and scheme of the scanning patterns used for glide path measurements (right)

During the trial, the averaged measurement range of the LIDAR was 8km which varied with weather conditions. The results show the capability of the LIDAR and of the dedicated post-processing to provide 3D volume wind data and glide path win data with an accuracy of 0.5m/s compared to the reference wind measurements from the vertical LIDAR profiler and from the research aircraft.

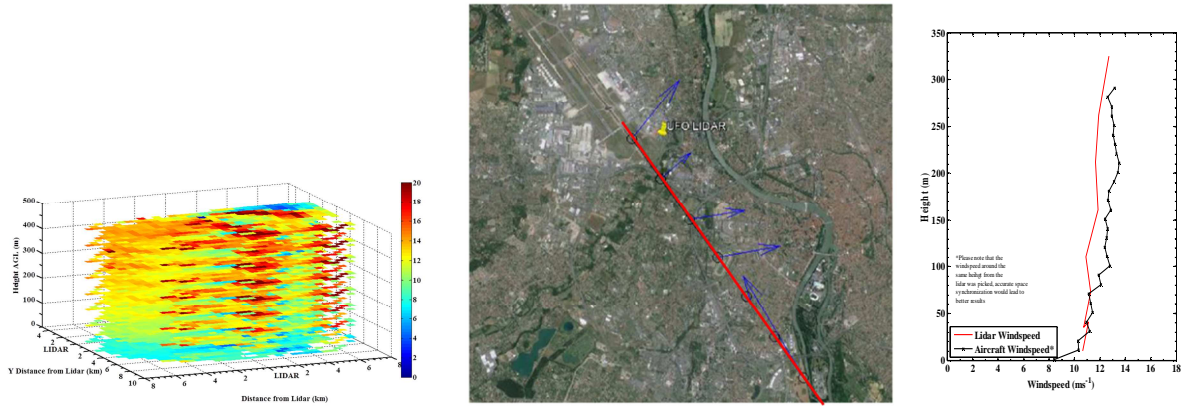


**Fig. 23** – Examples of volume wind data (left), glide path wind data (middle) and their accuracy compared to the research aircraft (right)

EDR retrieval has also been performed on LIDAR data. A preliminary example is given below for one of the scenario scan along the glide path (PPI with an elevation of  $4.6^\circ$  and azimuth  $180^\circ$  to  $208^\circ$ ), as a function of time, and for different altitudes. Structure functions are averaged over 10 minutes periods. The results show that EDR is higher at lowest altitudes in the surface layer as expected and showed in Fig. 24. Quantitative comparisons with reference sensors are on-going.

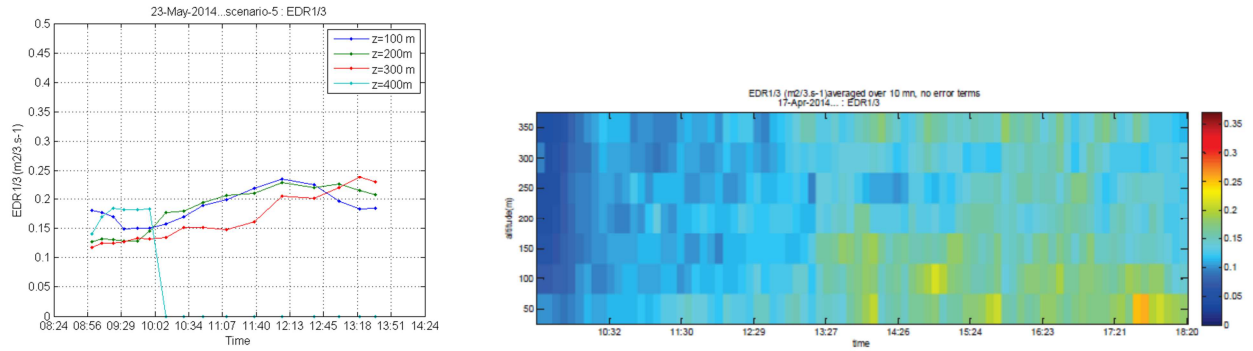


**Fig. 24** –EDR (left) as a function of altitude and evolution of EDR versus time and altitude (right)

The capacity of RADAR and LIDAR profilers to estimate turbulence intensity was evaluated prior to Toulouse Trials to calibrate algorithms with a test campaign during the 2013 summer at the Météo France facility of Trappes, near Paris. Simultaneous measurements of wind velocity were performed by both the CURIE X band RADAR and a WindCube v2 LIDAR from LEOSPHERE. The aims of such a campaign were three fold: first, to implement algorithms for estimating EDR from LIDAR and RADAR measurements, second to compare independent estimates from these two instruments, and third to assess the capacity of the two instruments to estimate EDR in various weather conditions. The EDR estimated from RADAR and LIDAR profilers are to be used as references for the Toulouse trials. The two instruments provide different measurements: either Doppler spectra every 3 or 6 s for the RADAR, or time series of radial velocities along five beams directions with a sampling period of 4 s for the LIDAR. It is thus necessary to develop different methods in order to retrieve turbulence parameters.

Time series of turbulence intensity obtained simultaneously by RADAR and LIDAR measurements on August 8th 2013 are shown in **Fig. 25**. An overall good agreement is found. EDR estimates range from  $10^{-6}$  to  $10^{-2} m^2 s^{-3}$ , i.e.  $0.01 \leq \varepsilon_k^{1/3} \leq 0.22 m^{2/3} / s$ , such values corresponding to light to moderate turbulence levels. One however observes some discrepancies between the LIDAR and RADAR EDR estimates, these differences sometimes reaching one order of magnitude (see **Fig. 25**) during the early morning).



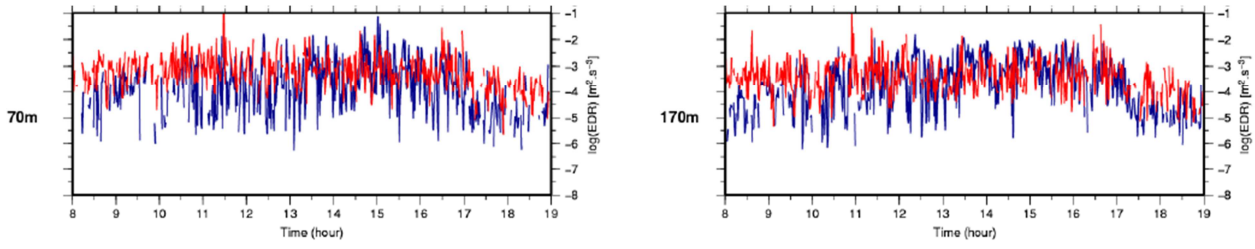


**Fig. 25** – Comparison of the eddy dissipation rates from CURIE RADAR (blue) and windcube LIDAR (red) at altitudes 70 and 170 m from 0800 to 1900 UTC the 8 August 2013.

Both RADAR and LIDAR measurements reveal the diurnal cycle of turbulence intensity based on EDR estimates (**Fig. 26**). The magnitude of EDR are close one to the other although discrepancies exist. Such discrepancies, likely partly due to differences in the criteria for selecting inertial turbulence motions, have to investigate. It is noticeable however that convection clearly develops over the entire measurement range during daytime at Trappes as showed in Fig. 26.

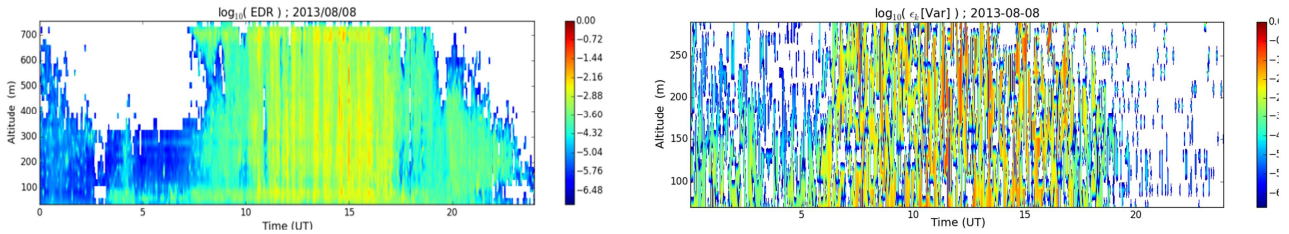


**Fig. 26** – Diurnal cycle of turbulence intensity as observed from the CURIE RADAR (left) and WindCube LIDAR (right)

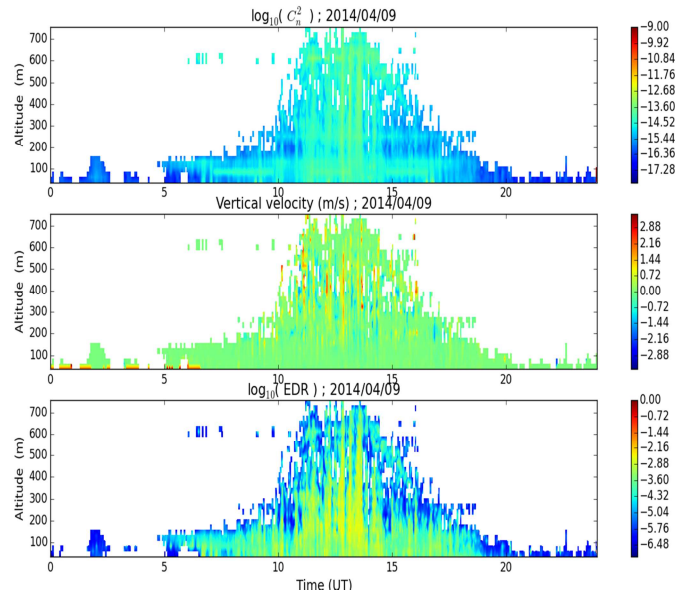


**Fig. 27** – Diurnal cycle of turbulence intensity and vertical velocity observed by CURIE RADAR at Toulouse airport on August 8th, 2014:  $C_n^2$  (top),  $w$  (central) and EDR (bottom).

Fig. 27 show typical diurnal (24h) space-time distributions of turbulence intensity as observed by the CURIE RADAR during the Toulouse airport trial. The top panel shows the refractive index turbulence ( $C_n^2$ ), the central panel showing the vertical velocity, whereas the bottom panel shows EDR. For this particular day, the convection appears much weaker

than for the Trappes example shown in Fig. 3. Despite this difference, EDR levels are found to be quite similar at both sites, i.e.  $0.01 \leq \varepsilon_k^{1/3} \leq 0.2 \text{ m}^{2/3}/\text{s}$ .

The inter comparison of several estimates (i.e. methods) for EDR show a good consistency, thus validating the underlying hypothesis of an inertial domain of fluctuations. Then, the comparison between LIDAR and RADAR estimates show an overall good agreement although some discrepancies still need to be clarified. Beyond these difficulties of interpretation, the ability of these instruments to measure turbulence in the atmospheric boundary layer is now demonstrated.

## 5. Airborne LIDARs

### 5.1. Airborne wake-vortex measurements

For airborne detection, the LIDAR must be able to detect the wake vortices generated by the previous aircraft. Wake vortex axial detection is more difficult because the radial velocity components (the projections of the 3D air velocity on the LIDAR beam axis) are very low. Instead of radial velocity, it is easier to detect the spectral broadening due to vortex turbulence

LIDAR systems used to date are based on solid-state laser do not meet commercial aircraft requirements for on board implementation due to high power consumption, size, weight, reliability, and life cycle cost. It was therefore the purpose of FIDELIO European project to introduce a unique fiber laser technology geared for the aerospace industry requirements, enabling onboard realization of an atmospheric hazard detection LIDAR system.

A pulsed laser allows the wind field to be spatially resolved along its line of sight, and scanning of the laser (e.g. the sinusoidal scan of Fig. 28 allows for the generation of an accurate 3D velocity image of the wind field.

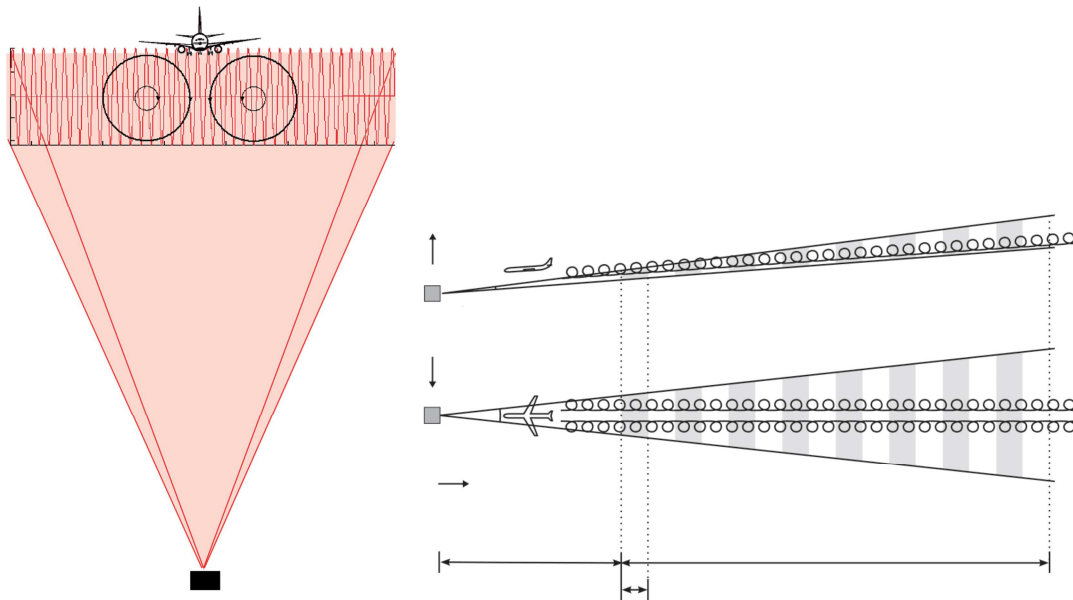


**Fig. 28** – ( Right ) : example of LIDAR scan for axial detection of wake vortices. ( Left ) experimental set-up for ground demonstration of onboard wake vortex LIDAR measurements

The purpose of the FIDELIO European project is to introduce a unique fiber laser technology geared for the aerospace industry requirements, enabling onboard realization of an atmospheric hazard detection LIDAR system. The FIDELIO LIDAR measures wind tracer velocities using coherent detection and a fiber architecture based on mainstream telecommunications components. The goal is to detect wake vortices along their axis at a range of 2 km. In-flight

demonstration of axial wake vortex detection was done during the IWAKE UE program [39][40]. FIDELIO project activities encompass the fiber laser design, the LIDAR simulations and design, and the field tests at Orly airport. A detailed presentation is available in [40].

During FIDELIO, extensive simulation has been performed in order to specify an adequate laser. Onera has developed an end-to-end simulation tool including the observation geometry, the wake vortex velocity image, the scanning pattern, the LIDAR instrument, the wind turbulence outside the vortex, and the signal processing. A simulation of large aircraft wake vortex evolution in a turbulent atmosphere has been performed by UCL/TERM. The simulation's main conclusion is that the pulse duration must be at least 800ns. A 1600 ns pulse gives very good simulation results but was not chosen for the LIDAR design because such a large range gate (240m) would lead to a system sensitive to wind gradient. Extensive simulations were carried out with varying laser energy  $E$ , pulse duration, PRF, and turbulence strength. The main conclusions are: - At medium range ( $>1\text{km}$ ), the vortex is easier to detect by measuring the spectrum broadening. These results confirm the IWAKE conclusions [33].

- Longer pulse duration (800 ns) gives better results than the nominal value of 400 ns and leads to a high velocity resolution.

- The vortex is easier to detect at old ages than at young ones, since dissipation increases the velocity dispersion on the observation axis. - Low PRF cannot be compensated for by increasing the laser energy. Indeed a high PRF value enables incoherent summation, reduced speckle effects and therefore a better velocity resolution. - For PRF = 4 kHz,  $E = 1\text{ mJ}$ , and nominal atmospheric conditions the theoretical LIDAR range is 2400 m. For PRF = 10 kHz and  $E = 0.1\text{ mJ}$ , the theoretical LIDAR range is 1200 m.

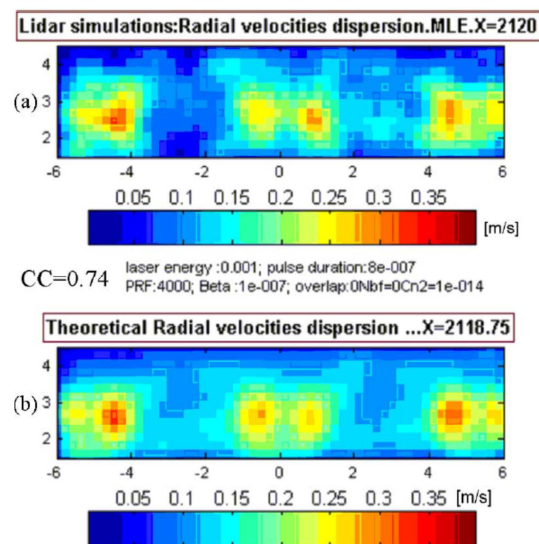


**Fig. 29** - LIDAR simulation images using the following parameters: pulse energy  $E = 1\text{ mJ}$ ; pulse duration of 800 ns; pulse repetition frequency of 4 kHz; atmospheric backscattering coefficient  $\beta = 1 \times 10^{-7}\text{ m}^{-1} \cdot \text{sr}^{-1}$ ; atmospheric turbulence  $Cn2 = 1 \times 10^{-14}\text{ m}^{-2/3}$ ; range gate of 2120 m. The value of the correlation coefficient for this image is  $CC = 0.74$ .

Detection range during field test from Orly was in accordance with simulation results [40].

## 5.2. Airborne Clear Air Turbulence measurements

A whole class of turbulence events, designated as Clear Air Turbulence, cannot be detected by any existing airborne equipment, including state of the art weather RADAR. This kind of turbulence is linked to large amplitude gravity waves (downstream to mountains for example) or to strong vertical shear of horizontal wind (Kelvin-Helmoltz instabilities).

Long-range avoidance of turbulence encounter requires systems with maximal range larger than 30 km which cannot be fulfilled by LIDAR system with acceptable size and power consumption for airborne operation. Medium and short range systems have been studied in order to have the seat belts fasten before encounter or to mitigate the turbulence effects by flight controls. In the first case, the turbulences have to be detected and a severity and range have to be assessed (thus requiring range from 8 to 30 km). In the latter case, a three axis air speed has to be measured in order to be used in the flight control systems (requiring typical range of 50-300 m). In that case, the function becomes critical (since it is used in the flight controls). The UV direct detection Rayleigh LIDAR is a good candidate for medium range and short-range operations [41][42][43][44].

The medium-range CAT detection is based on air density fluctuations measured through backscattered energy fluctuations of the LIDAR signal [41][42]. The RMS fluctuations of temperature and density are statistically linked with the RMS fluctuations of the vertical speed according to the relation:  $\frac{\delta \rho(x)}{\rho} = -\frac{\delta T(x)}{T} = \frac{N}{g} w(x)$

where  $N$  is the Brunt-Väisälä angular frequency ( $N \sim 0.01$  rad/s in troposphere and  $N \sim 0.02$  rad/s in stratosphere) and  $g$  is the gravity acceleration, giving rise to maximum density fluctuations of the order of the percent.

A processing of LIDAR signal must be performed to deduce from the measurement the molecular back-scattering coefficient.

The short-range operation is based on 3 axis wind velocity measurement ahead of the aircraft, obtained by spectral analysis of the Doppler shift of backscattered LIDAR signal [43][44]. Despite the fact that the collecting cone is nearly four orders of magnitude larger at short range than at long range, the photon budget of the short-range operation is quite challenging due to the short integration time and the required accuracy.

Interferometers can be used for the spectral analysis of the backscattered light both with imaging [43][44] or filtering principles. In the first principle, the image analysis of the interference pattern (fringes or rings) allows the determination of the radial wind speed with a measurement accuracy that is even better when aerosol back scattering is significant.

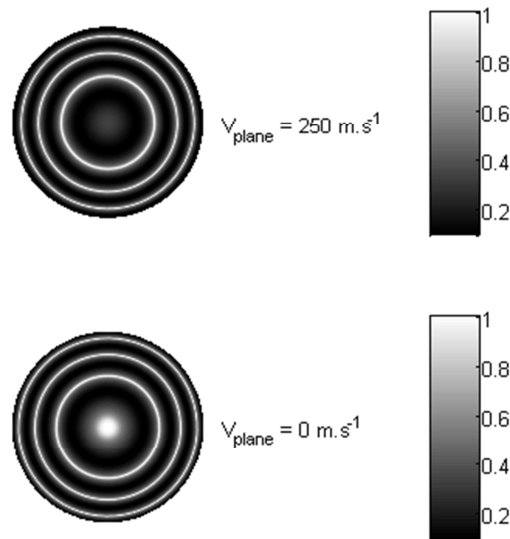


**Fig. 30.** - Example of double ring interference from the analysis of aerosol and molecular backscattering in UV (355 nm). The aerosol backscattering leads to narrow rings (due to reduced spectral width of the backscattered spectrum associated with aerosol mass) and the molecular backscattering leads to larger rings (spectral width of molecular backscattering is in the range of 2 GHz).

Using filtering principle, the molecular spectrum can be reconstructed using a reduced number of spectral channels. One of the studied solutions consists in filtering the backscattered spectrum using two slightly shifted Fabry Perot interferometers. Typical spectra of the two channels are shown in Fig. 31 with the back-scattered spectrum.

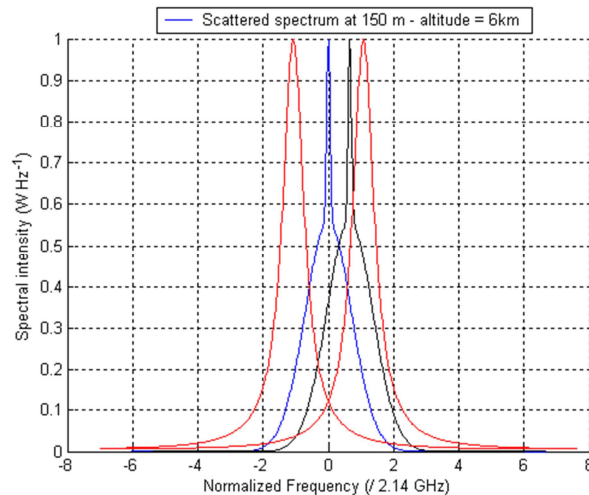


**Fig. 31** - Typical backscattered spectrum at 355 nm analysed using a double edge Fabry Perot analysis. Transmission of the two Fabry Perot interferometers (red) – Back-scattered spectrum at 0 m.s<sup>-1</sup> (blue) – Back-scattered spectrum at 250 m.s<sup>-1</sup> (black)

This approach can be made insensitive to aerosol (Mie) scattering by a careful design: scattering ratio sensitivity can generally be minimized with optimal parameters. Temperature and pressure sensitivity may in principle be compensated for with proper in-situ air-temperature and pressure measurement.

Polarization measurements are an alternative / complementary method to discriminate between aerosols and molecules scattering. Flight tests have been realized within FP7 project DELICAT during July and August 2013 [51]. A UV LIDAR has been tested on-board a Cessna Citation II at various locations over Europe (see [51] for details). It has been decided to use for these flight tests a two-channel polarization measurement, with a linearly polarized emission light. Backscattering on molecules is known to lead to very low depolarization (less than 1%). Moreover, backscattering on aerosols whose size is of the order of magnitude of the wave-length are known to show significant depolarization. A complete processing chain was designed to exploit the recorded two channels LIDAR signals (co- and cross-polarized to the emitted laser pulse). The principal steps of this chain are:

- Normalization. The LIDAR signals are the product of the fluctuating backscattering strengths of interest and of a smooth function resulting for attenuation, geometrical spreading and LIDAR overlap. This function is estimated through a time averaging over few minutes. The signals are then divided by this function.
- Shifting. After normalization, the signals present slant features, reflecting the advance of the A/C, as shown in Fig. 33. In order to accumulate information on specific absolute locations in space, the signals have to be shifted and interpolated on a fixed grid, taking into account the variable True Air Speed of the plane. This is realized at specific evaluation times at which the situation in front of the plane is assessed, typically every 1 km.
- Estimation of backscattering strength coefficients. The signals recorded for each emitted pulse present a large amount of noise, either photon noise or receiver noise. In order to estimate the backscattering coefficients, one has to perform some weighted average of the individual measured coefficients (normalized and shifted signals).

We choose to realize a maximum likelihood estimation of these coefficients, in which the weights are inversely proportional to the variance of the corresponding measurements, and then decrease with increasing sampling distance. A procedure has been implemented in which at a given absolute sampling distance, the variance of the measurements are estimated as a function of recurrence time.

This estimator minimises the variance of the estimated parameters. Moreover, the variance always decreases with increasing number of measurements, whatever their variances, so that in principle the integration time has not to be bounded. This has to be tempered by the following considerations:

- The estimation procedure relies on the assumptions of frozen turbulence on one hand and of constant LIDAR axis on the other hand. Model errors then superimpose to detection noise.
- The variances themselves have to be estimated, leading to additional errors.

In practice we have used an integration time corresponding to A/C displacement between 2 and 4 km. With signal length slightly above 15 km, an integration distance of 4 km gives a maximum detection distance slightly below 11 km (due to variance computation length).

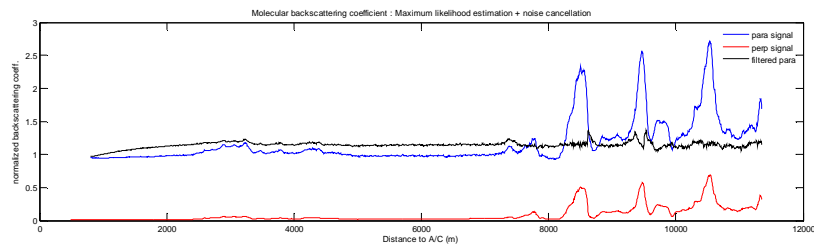


**Fig. 32**– Example of the effect of noise cancellation on the estimated backscattered strengths, cross-polarized channel (red) – co-polarized channel (blue) – co-polarized channel after aerosol contribution cancellation (black)

- Aerosols contribution elimination. The CAT detection principle implemented in DELICAT is to detect the small fluctuations, associated to turbulence-induced density fluctuations, of the Rayleigh scattering contribution to the LIDAR signal. The part of the co-polarized channel signal that is not correlated to cross-polarized one is attributable to molecules or at least to very small (with respect to the wave-length) or spherical particles. The technique, which consists to remove from a signal a component that is correlated to a reference noise (here the cross-polarized signal) is known as noise cancellation. This is realized through an adaptive filtering in which a filter of the reference noise is searched by minimising an error function. This error function is the power density of the signal itself from which is subtracted the filtered noise. An example of result of this filtering is shown on Fig. 32. The large bumps of the co-polarized signal, highly correlated to the cross-polarized one, are almost removed. In general, the contributions of aerosols in the co-polarized channel are largely reduced with this technique, due to scales of variation of their concentrations larger than those of density fluctuations. Nevertheless, complete “cleaning” of the Rayleigh signal seems not achievable in all situations without the use of a spectral filter.
- Thresholding of the standard deviation of the signal. The filtered co-polarized signal is then processed to exhibit features that are supposed to be highly correlated to the presence of turbulences. The basic idea is to detect high values of the local variance of the signal, while eliminating all the causes of high local variances not related to turbulences. The signal is analysed with a sliding window whose width is typically a few hundreds of meters (800 m in the example shown latter). Possible removal of the linear component of the signal in each window is important since the analysed signal sometimes exhibits large scale oscillations, the origin of which is difficult to determine. Without removal of the linear component, the subsequent detection of large values of the variance will in fact detect the fronts of these oscillations, which are not necessarily related to turbulences. Alarms are set if these conditions are met:
  - A predefined threshold is exceeded over a distance greater than a specified value, set to 400 m (to limit false alarms).
  - The mean depolarization ratio is less than a specified value. This value has been set to 0.1, which may seem high but reflects the fact that the cross-polarized signal may be dominated by detection noise at large distance.
- Tracking. In the detection signal processing suite, the situation is evaluated at regular time intervals, of the order of 5 s corresponding to a detection sampling distance  $D_s$  (travel distance of the A/C about 1 km). The evaluation is based upon the signals recorded on a flight distance  $D_i$ , typically set to 4 km. In order to reduce false alarms and to take advantage of the possible coherence among successive evaluations, an effective standard deviation function at a new sampling distance is computed as a weighted mean of the measured standard deviation at the new distance and of the shifted effective one at the previous distance. The weighs correspond to exponential fading with a characteristic memory distance  $D_m$  which is chosen of the same order of magnitude than  $D_i$ .



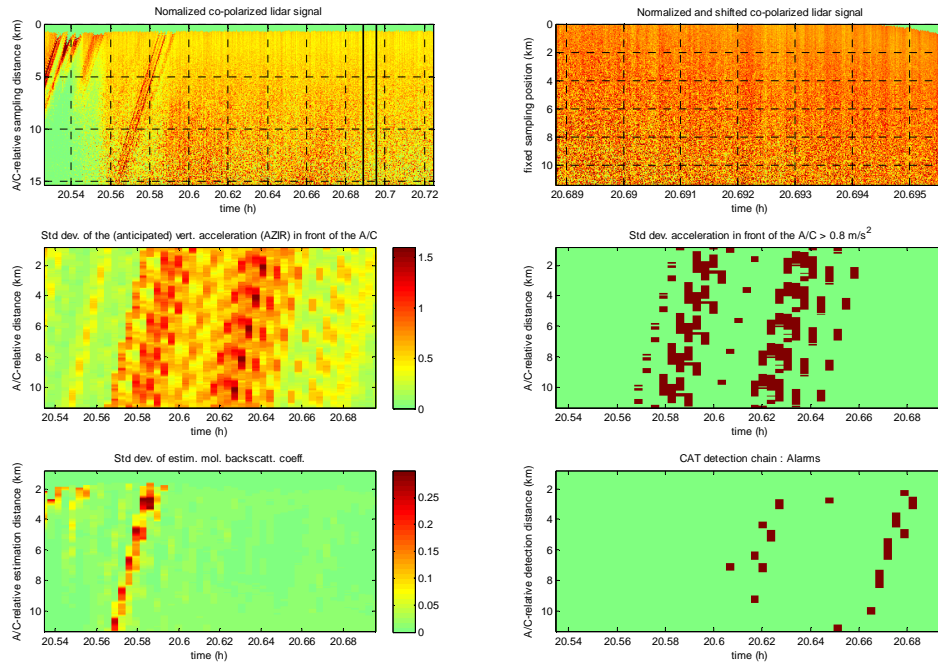


**Fig. 33** : Example of CAT detection on flight test data (see text)

An exemple of application of the signal processing chain on data recorded during a flight test is shown in Fig. 33. The upper left figure shows the co-polarized normalized signal, with horizontal axis representing emission time and vertical axis representing the sampling distance in front of the A/C. Large amounts of aerosols are visible at the beginning of the sequence, with very low levels behind the aerosols. The upper right figure shows the current analysed zone represented between black lines of the left figure (in this case it is the last analysed zone).

The middle left figure represents the standard deviation of the acceleration in front of the plane as it is measured (AZIR) when the A/C fly at this location. This representation, in post processing, is for direct comparison with corresponding lidar detection.. The middle right figure corresponds to an all or nothing representation of the standard deviation of the same acceleration with a threshold which is set here at  $0.8 \text{ m/s}^2$ .

The lower left figure standard deviation of the estimated molecular backscattering strength coefficient and the lower right figure gives the alarms of the detection chain.

At the beginning of the sequence the variability of the signal is dominated by the effect of aerosols but this does not give rise to false alarms due to the constraints on the depolarization ratio and on the amplitude of the fluctuations.

The turbulence burst arising at 20.6 h is not detected, because it appears in the LIDAR signal before the strong aerosol encounter has disappeared, so a more refined algorithm would be necessary. Later, two bursts of turbulences are detected. The first one has a maximum local value of the acceleration about  $3 \text{ m/s}^2$  and maximum standard deviation is about  $1.5 \text{ m/s}^2$ . It corresponds to a “light turbulence” according to the AMDAR Reference Manual – WMO n°958 - severity scale (Peak acceleration between 0.15 g and 0.5 g). The second one is very light with a peak acceleration of  $1 \text{ m/s}^2$  (referred to as “none turbulence” in the previously mentioned severity scale. However these detections are associated to large amplitude variations of the co-polarized signal that not seem compatible with density variation associated to CAT (expectation value about 1%). These detections generally disappear when the linear component of the signal is removed before estimation of its standard deviation. Nevertheless, the detected fronts are often located where the turbulence burst lies but there is no known explanation for this coincidence. During the flight tests, only light turbulences were encountered and more data with larger turbulences events would be necessary to fully assess the capability to detect CAT with polarization measurements.

It remains that the detection of CAT lying in depolarizing aerosols seems difficult with this technique alone. Noise cancellation helps but does not seem sufficient in all the situations, so that the use of a spectral Mie-Rayleigh separation filter, as described in the beginning of this section and more difficult to implement in operational conditions, would be very useful.

## 6. Conclusions and perspectives

New RADAR and LIDAR remote sensor technologies have been developed for improving air traffic safety and operations. This paper describes how wind, eddy dissipation rate (EDR) and wake vortices can be measured with ground based scanning or profiling remote sensor like 1.5micron LIDARs and X-band RADARs. Accurate 3D Wind measurements can be provided by scanning LIDAR in comparison with reference wind sensors. EDR can be retrieved from LIDAR or RADAR sensors with different methods. The preliminary analyses show good agreements between the vertical RADAR and LIDAR profilers and the feasibility to provide maps of EDR. Wake vortices can be monitored by LIDAR and RADAR. High sensitivity of the effect of wake vortices on raindrops has been observed. Thanks to the good range resolution (5 m), accurate discrimination of the 2 vortices, even for small aircrafts has been obtained. RADAR performances are optimal under rainy/humid conditions whereas LIDAR performances are optimal under clear air conditions. The combined LIDAR + RADAR system provides the capability to detect wake-vortex in all-weather conditions. X-band RADAR and 1.5micron LIDAR will be deployed during 1 year at Paris CDG airport to provide statistical figures of their performances in different weather conditions.

In terms of perspectives, the assessment of the accuracy of winds, EDR and wake vortices will be performed for the RADAR and LIDAR with regards to the strength of the signal and to the weather conditions. An in-depth analysis will be performed in order to determine the area of operations of both sensors to optimize their combination and ensure the development of an all-weather wake vortex advisory system that is mandatory for the future concepts of weather dependent separations. Wake turbulence problematic strengthens the demands for on-board advisory systems of wake vortex or even clear air turbulence. Previous studies based on airborne UV LIDARs and IR LIDARs showed promising results for wake vortices and clear air turbulence measurements at high altitudes. New studies are required to determine the functional needs from the pilots and aircraft points of view in order to determine the most appropriate sensor technology.

## 7. Acknowledgments

These studies have been funded by UFO EU FP7 R&D Program, SESAR EU Program, DELICAT FP7 EU project, FIDELIO FP6 EU, ONERA & ISAE have developed the RADAR simulator in rain calibrated with Thales X-band RADAR data, ONERA has developed the RADAR simulator in clear air.

UFO (Wind/EDR Monitoring) Website: <http://www.ufo-wind-sensors.eu/home>

## 8. References

- [1] The CREDOS Project D2-6 - WP2 Final Report, CREDOS European project, August 2009 - <https://www.eurocontrol.int/sites/default/files/content/documents/sesar/credos-d2-6-wp2-final-report-v11.pdf>
- [2] Dolfi-Bouteyre, A.; Canat, G.; Valla, M.; Augere, B.; Besson, C.; Goular, D.; Lombard, L.; Cariou, J.-P.; Durecu, A.; Fleury, D.; Bricteux, L.; Brousmiche, S.; Lugan, S.; Macq, B., "Pulsed 1.5-  $\mu\text{m}$  LIDAR for Axial Aircraft Wake Vortex Detection Based on High-Brightness Large-Core Fiber Amplifier," Selected Topics in Quantum Electronics, IEEE Journal of, vol.15, no.2, pp.441,450, March-april 2009
- [3] S. Kameyama, T. Ando, K. Asaka, Y. Hirano, and S. Wadaka, "Compact all-fiber pulsed coherent Doppler LIDAR system for wind sensing", Appl. Opt. 46, 1953-1962 (2007).
- [4] X. Zhang, W. Diao, Y. Liu, J. Liu, X. Hou and W. Chen, "Single-frequency polarized eye-safe all-fiber laser with peak power over kilowatt", Applied Physics B, pp. 1-5 (2013).
- [5] J.-P. Cariou, B. Augere, M. Valla, "Laser source requirements for coherent LIDARs based on fiber technology", Comptes Rendus Physique, Volume 7, Issue 2, March 2006, Pages 213-223.
- [6] Al-Sakka H., Weil A., Le Gac C., Ney R., Chardenal L., Vinson J.P, Berthès L. and Dupont L., 2009, CURIE: a low power X-band, low atmospheric Boundary Layer Doppler RADAR, Meteorologische Zeitschrift, Vol. 18, No. 3, pp. 267-276
- [7] Cariou J.P., Boquet, M., "Pulsed LIDAR Principles, Contribution to UpWind WP6 on Remote Sensing Devices"
- [8] Doviak RJ, Zrnic DS. Doppler RADAR and Weather Observations, 2nd ed. Academic Press, 1993, 304 pp.

- [9] Chan PW, Shao AM. Depiction of complex airflow near Hong Kong International Airport using a Doppler LIDAR with a two-dimensional wind retrieval technique. *Meteorologische Zeitschrift* 2007; 16: 491–504.
- [10] Krishnamurthy R., Coherent Doppler LIDAR for wind farm characterization, *Wind Energ.* (2012), DOI: 10.1002/we.539, RESEARCH ARTICLE
- [11] Kongara S, Calhoun R, Choukulkar A, Boldi M. Velocity retrieval for coherent Doppler LIDAR. *International Journal of Remote Sensing* 2011; In Press.
- [12] Xu Q, Gong J. Background error covariance functions for Doppler radial-wind analysis. *Quarterly Journal of the Royal Meteorological Society* 2003; 129: 1703–1720.
- [13] Chan P. W., Lee Y. F., Performance of LIDAR- and RADAR-based turbulence intensity measurement in comparison with anemometer-based turbulence intensity estimation based on aircraft data for a typical case of terrain-induced turbulence in association with a typhoon”, *J Zhejiang Univ-Sci A (Appl Phys & Eng)* vol.14 n7, pp.469-481, 2013
- [14] Frehlich R, Yannick M, Michael LJ, Ben B, Sharman R., Measurements of boundary layer profiles in an urban environment. *Journal of Applied Meteorology*, n°45, pp.821–837, 2006
- [15] Banakh VA, Smalikho IN. (1997). Estimation of turbulent energy dissipation rate from data of pulse Doppler LIDAR. *Journal of Atmospheric and Oceanic Optics* 10: 957–965.
- [16] Frehlich R, Hannon S, Henderson S. (1998). Coherent doppler LIDAR measurements of wind field statistics. *Boundary-Layer Meteorology* 86: 233–256.
- [17] Nastrom, G. (1997). Doppler RADAR spectral width broadening due to beamwidth and wind shear. *Ann. Geophysicae*, 15:786–796.
- [18] Wilson, R., Turbulent diffusivity in the free atmosphere inferred from MST RADAR measurements: a review, *Ann. Geophys.*, 22 (11), 3869-3887, 2004
- [19] Chan et al. , Performance of LIDAR- and radar-based turbulence intensity ..., *J Zhejiang Univ-Sci A (Appl Phys & Eng)* 2013 14(7):469-481
- [20] David Keith Wilson, “Three Dimensional Correlation and Spectral Functions for Turbulent Velocities in Homogeneous and Surface-Blocked Boundary Layers”, technical report of the Army Research Laboratory ARL-TR-1287, July 1997
- [21] Frisch, A. S. and Clifford, S. F. (1974). A study of convection capped by a stable layer using Doppler RADAR and acoustic echo sounders. *J. Atmos. Sciences*, 31:1622–1628.
- [22] Gossard, E. E., Wolfe, D. E., Moran, K., Paulus, R. A., Anderson, K. D., and Rogers, L. T. (1998). Measurement of clear-air gradients and turbulence properties with RADAR wind profilers. *J. Atmos. Oceanic Technol.*, 15:321–342.
- [23] Jacoby-Koaly, S., Campistron, B., Bernard, S., Bénech, B., Arduin-Girard, F., Dessens, J., Dupont, E., and Carissimo, B. (2002). Turbulent dissipation rate in the boundary layer via UHF wind profiler Doppler spectral width measurements. *Boundary-Layer Meteorol.*, 103:361–389.
- [24] Bouniol, D., Illingworth, A. J., and Hogan, R. J. (2003). Deriving turbulent kinetic energy dissipation rate within clouds using ground based 94 ghz RADAR. Preprints, 31st Conf. on RADAR Meteorology, Seattle, WA, Am. Meteor. Soc., 18:193–196. available at: <http://ams.confex.com/ams/pdfpapers/63826.pdf>.
- [25] O'Connor, E. J., Illingworth, A. J., Brooks, I. M., Westbrook, C. D., Hogan, R. J., Davies, F., and Brooks, B. J. (2010). A method for estimating the turbulent kinetic energy dissipation rate from a vertically pointing doppler LIDAR, and independent evaluation from balloon-borne in situ measurements. *J. Atmos. Oceanic Technol.*, 27:1652–1664.
- [26] Shupe, M. D., Brooks, I. M., and Canut, G. (2012). Evaluation of turbulent dissipation RADAR retrievals from Doppler cloud RADAR. *Atmos. Meas. Tech.*, 5:1357–1385.
- [27] White, A. B., Latatit, R. J., and Lawrence, R. S. (1999). Space and time filtering of remotely sensed velocity turbulence. *J. Atmos. Oceanics Technol.*, 16:1967–1972.
- [28] Kelly A.J., Handelsman M., 1974, Electromagnetic effects of aircraft wake-active feuillet interaction, *IEEE Transaction on Aerospace and Electronic Systems* , Vol. 10 n°1, pp.136–143
- [29] Gilson W.H. , 1994, Aircraft Wake RCS measurement, In *NASA Contractor Rep.* 10139, Part 2, pp.603-623
- [30] Shariff K. , 2002, Analysis of the RADAR Reflectivity of Aircraft Vortex Wakes, *J. Fluid Mech.*, vol.463, pp.121-161
- [31] Friedrich Kopp, etAl , “Characterization of aircraft wake vortices by 2-micro pulsed doppler LIDAR,” *Journal of Atmospheric and Oceanic Technology*, vol. 21, no. 2, pp. 194–206, 2004.
- [32] D Jacobs et Al, “Assessment of Lockheed Martin aircraft wake vortex circulation estimation algorithms using simulated LIDAR data,” in *3rd AIAA Atmospheric Space Environments Conference*, Honolulu, HI (submitted for publication), 2011.
- [33] D. Douchamps, Y. Verschuere, S. Lugan , L Mutuel, B. Macq and K. Chihara - On-board axial detection of wake vortices using a 2µm Lidar. *IEEE Trans. on Aerospace and Electronic Systems*, vol. 44, No. 4 (2008).
- [34] Agnes Dolfi-Bouteyre et al., “1.5µm all fiber pulsed LIDAR for wake vortex monitoring,” in *Conference on Lasers and Electro-Optics*. Optical Society of America, 2008, p. CMQ3.
- [35] A Dolfi-Bouteyre & Al Aircraft Wake Vortex Study and Characterization with 1.5 µm ..., [www.aerospacelab-journal.org/...aerospacelab.../A11-.2009](http://www.aerospacelab-journal.org/...aerospacelab.../A11-.2009)

- [36] Rod Frehlich and Robert Sharman, "Maximum likelihood estimates of vortex parameters from simulated coherent doppler lidar data," *Journal of Atmospheric and Oceanic Technology*, vol. 22, no. 2, pp. 117–130, 2005
- [37] Monin A. S. & Yaglom A.M. , *Statistical fluid mechanics : Mechanics of turbulence – Vol 2*, The MIT Press , 1975
- [38] Kolmogorov, A. N., "The local structure of turbulence in incompressible viscous fluid for very large Reynolds numbers", *Proceedings of the USSR Academy of Sciences (in Russian)* 30: 299–303, 1941
- [39] Tani T. & Bertin F., 1992, *Restitution en temps réel du champ de vitesses créé par des vortex d'avions*, CNRS/CRPE & STNA report
- [40] Rat G. & Bertin F., 1992, *Etude théorique de la détection des vortex générés dans le sillage des avions à l'aide d'un RADAR*, CNRS/CRPE report
- [41] Feneyrou P., Leheureau J-C., Barny H., Performance evaluation for long-range turbulence-detection using ultraviolet LIDAR, , *Applied Optics*, Vol. 48, Issue 19, pp. 3750-3759 (2009)
- [42] Vrancken P., Wirth M., Rempel D., Ehret G., Dolfi-Bouteyre A., Lombard L., Gaudo T., Rees D., Barny H., Rondeau P., *Clear Air Turbulence detection and characterization in the DELICAT airborne LIDAR project*, 25th International Laser RADAR conference, 5-9 July 2010, St.Petersburg, Russia
- [43] Cézard N., Dolfi-Bouteyre A., Huignard J.P., Flamant P. H., Performance evaluation of a dual fringe-imaging Michelson interferometer for air parameter measurements with a 355 nm Rayleigh–Mie LIDAR, *Applied Optics*, Vol. 48, Issue 12, pp. 2321-2332 (2009)
- [44] Guillermo Jenaro Rabadan, Nikolaus P. Schmitt, Thomas Pistner, Wolfgang Rehm ,*Airborne LIDAR for Automatic Feedforward Control of Turbulent In-Flight Phenomena*, , *Journal of Aircraft*. 01/2010; 47(2):392-403.
- [45] L.J.P. Speijker, F. Barbaresco, M. Frech, A. Vidal, G. Winckelmans & H. Barny, "ATC-Wake : Integrated Wake Vortex Safety & Capacity System", *Journal of Air Traffic Control*, Volume 49, No 1, pp.17-32, April 2007
- [46] G. Winckelmans, F. Barbaresco & al. "The ATC-Wake Predictor system and its potential use to increase the capacity at airports", *JISSA Conf.*, 20 - 21 June 2005, Paris, France.
- [47] Barbaresco F., 2013, *Compréhension et maîtrise des tourbillons de sillage. Cinq siècles d'aventures de Léonard de Vinci à Jean Leray*, *Revue REE*, n°3, pp.84-88
- [48] Steen M., Schönhals S., Polvinen J., Drake P., Cariou J.P., Dolfi-Bouteyre A., Barbaresco, F. , 2010, *Airport Radar Monitoring of Wake Vortex in all Weather Conditions*, Eurocontrol 9th Innovative Research Workshop & Exhibition
- [49] Vanhoenacker-Janvier D., Djafri K., della Faille de Leverghem R., van Swieten B., Barbaresco F., 2012, *Simulation of the Radar Cross-Section of Wake Vortices in clear air*, ERAD'12 Conference, Toulouse
- [50] Barbaresco F., Juge P., Klein M., Canal D., Ricci Y., Schneider J.Y., , Mutuel L., 2013, *Wake Vortex Detection, Prediction and Decision Support Tools In SESAR Program*, 32th DASC Conference Syracuse (Best Paper In The Emerging Technologies and Systems)
- [51] Flight Testing DELICAT – A promise for medium-range clear air turbulence protection, Veerman H.P.J., Vrancken P., Lombard L., *European 46<sup>th</sup> SETP and 25<sup>th</sup> SFTE Symposium*, 15-18 June 2014, Lulea, Sweden